

# 6

## Application of Results

### Introduction

In this concluding chapter the concepts developed for describing cross sections and rate constants are applied to a few of the problem areas discussed in Chapter 1. This discussion, being consistent with the rest of the text, is not intended to be a state-of-the art presentation on each topic and the ideas presented are, for the most part, well established. Further, the cross-section models used are quite simple. In the previous chapters the relationship between the simple and more accurate models for cross sections have been considered. Therefore, the reader should have a feel for the kinds of errors introduced by the choice of cross-section model and is encouraged to include improved estimates. Care should be taken that the increased complexity caused by using a more accurate approximation for cross section is warranted by the correctness of the description of the physical problem. In the following no statement is implied about this. I have only chosen models which lend themselves to either analytic solutions for the problem or to simplifying the presentation. This merely follows the lead of a number of authors who have made wide use of simple cross-sectional forms in discussing, for example, complex radiation transport problems. In many other cases I have simply taken results for certain rate constants generally used in the literature without further discussion, particularly for processes considered in Chapter 5.

The discussion in the following sections begins with a consideration of the penetration of fast particles into a material and the subsequent diffusion of these implanted particles. In addition, entering fast particles cause displacements in the material, which is discussed in the context of a problem from radiation biology, and also the very interesting phenomenon, sputtering. Sputtering involves the etching of the surface layer generally by fast-ion ejection of the target material. Up to this point it was assumed that the

material penetrated had a surface, and inside the surface a nearly constant density exists. Although this provides a certain simplicity, it is not a necessary restriction. Therefore, it is pointed out that similar ejection occurs in a planetary atmosphere in which the material is contained by gravity rather than the short-range atomic forces. The radiation primarily responsible for ejection now is "sunlight," although in some situations charged particles play a role. This leads quite naturally to the discussion of other processes induced by solar radiation, e.g., those chemical processes determining the density and constituents in the earth and Martian ionospheres.

### Energetic Particle Transport

Two cases of energetic particles traversing a material are shown in Figure 6.1. The first indicates the occurrence of a hot particle created in a material. This could be the result of the absorption of radiation (ultraviolet, X-rays, neutrons, etc.), a spontaneous fission, or because the atom of interest is set in motion by a collision with a fast particle. The second situation is the radiation example we considered earlier in which, typically, ions are incident on a material as in ion implantation experiments. These situations are not that different. In the second case the net effect will be a sum of the effects of the moving secondary particles created in the material. Differences arise, however, when one considers phenomena near the surface. In either case the first question one asks is how much of the material is affected by the particle or, on the average, how far does it travel.

To answer the above question a simulation procedure could be constructed in which the material atoms are assigned places, randomly for amorphous materials, or in an ordered manner for crystalline materials. The motion of the atom is then followed using the collision cross sections at each encounter of the moving atom with a material atom. The initial impact parameter is chosen randomly for the first collision. In Chapter 1 we took an alternate approach to case b in Figure 6.1, determining the partial

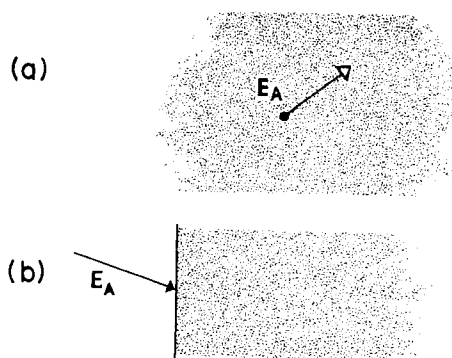


**Figure 6.1.** Events initiating a particle cascade. (a) Radiation created in a material; (b) radiation incident on a surface.

flux in the cascade, as a function of depth, from an integral equation. This procedure applies to amorphous materials or to crystalline materials for particles not moving along crystal planes. In many instances both of these procedures provide more detail than may be warranted. For instance, the mean penetration depth of an incident particle of energy  $E_A$  is

$$\bar{R}_p(E_A) = \iiint I(\mathbf{p}, z) z dz d^3p \quad (6.1)$$

using the solution to Eq. (1.2). However, solving for  $I(\mathbf{p}, z)$  to obtain  $\bar{R}_p$  would be superfluous. Therefore, we begin the discussion by considering a simpler, historically useful approach, and build upon it when more detail is required. We will ignore the simulation approach which, though straightforward, requires a large programming effort to calculate even rather simple quantities such as  $R_p$ .

### The Continuous Slowing-Down Approximation

Earlier in Eqs. (2.18) and (2.17) the energy loss per unit pathlength, the stopping power of the material, was defined in terms of a quantity called the stopping cross section,  $S_{AB}$ ,

$$-\frac{dE}{ds} \equiv n_B S_{AB} \quad (6.2)$$

where  $s$  is the path length and  $n_B$  the target number density. The energy loss processes are, as usual, separated into elastic collisions involving energy transfer to the target center of mass (the nuclei), and inelastic processes involving energy transfer to the electron, i.e.,

$$S_{AB} \simeq S_n + S_e$$

Equation (6.2) can be integrated directly to yield an estimate of the average path length traveled by the incident particle before stopping,

$$\bar{R}(E_A) = \int_0^{E_A} \frac{dE'}{n_B S_{AB}(E')} \quad (6.3)$$

This is the continuous slowing-down approximation (CSDA) to  $\bar{R}$ . That is, it is a calculation in which the energy is assumed to be dissipated continuously as in a drag force. For a particular choice of incident particle and target material, Eq. (6.3) can be integrated numerically using measured or calculated stopping cross sections. For our purposes the behavior of  $\bar{R}$  with energy can be investigated using the power law potentials of Chapter 2 either classically or in the Born approximation. The resulting electron or nuclear stopping cross section can be written as  $S_{AB} = \xi_x E_A^{1-x}$ , with  $x$

determined from the potential (e.g.,  $x = 2/n$ , classically). From the discussion and results in Chapter 5 for  $S_{AB}$ , we see that  $x$  is slowly varying in energy over broad regions in energy. Treating  $x$  as a constant over the predominant stopping region for each  $E_A$ , we have

$$\bar{R}(E_A) \sim \frac{1}{xn_B \zeta_x} E_A^x = \frac{E_A}{xn_B S_{AB}} \quad (6.4)$$

Therefore  $\bar{R}$  can be estimated from the size of  $S_{AB}$  and the slope of  $S_{AB}$  (e.g.,  $x$ ) at each energy. By fitting  $S_{AB}$  to an accurate result in the vicinity of  $E_A$  in order to obtain  $x$ , the approximation in Eq. (6.4) is compared in Figure 6.2 to a numerical integration over the stopping cross section shown. The mean range is seen to be monotonically increasing in energy, a not very surprising result, and the simple approximation is in reasonable agreement.

There are two errors in the above description. The first is the use of an oversimplified approximation to  $S_{AB}$ , which is easily remedied. The second arises from the fact that the target medium is not continuous, the targets are discrete, and the collisions occur statistically. This implies that there is a variation of the particle ranges from the mean range as each particle has a different history, that is, a different energy loss in each collision. The root-mean-squared deviation in the range,  $\overline{\Delta R}^2$ , in the CSDA approximation is determined from the mean-squared deviation in the energy transfer in an individual collision,  $S_{AB}^{(2)}$ . This quantity, referred to as the energy straggling cross section, has the form

$$S_{AB}^{(2)} \simeq \int \Delta E^2 (d\sigma/d\Delta E) d\Delta E \quad (6.5)$$

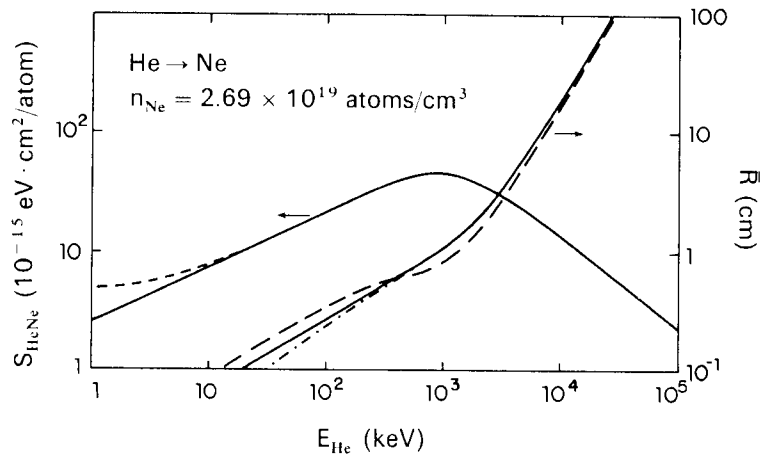


**Figure 6.2.** He  $\rightarrow$  Ne stopping for equilibrium charge state of He, (see Chapter 5; from J. F. Ziegler, *Helium: Stopping Powers and Ranges in All Elements*, Pergamon Press, New York (1978).  $S_{\text{HeNe}}$ : (left-hand scale) solid line, electronic; short-dashed line, electronic plus nuclear.  $R$ : (right-hand scale) solid line, accurate calculation using Eq. (6.13a) (with  $\cos \Theta_A = 1$ ); long-dashed line, using approximation to CSDA in Eq. (6.4);  $\bar{R}_p$ : (right-hand scale) dot-dashed line, using Eq. (6.13b).

For power laws, we have  $S_{AB}^{(2)} = \zeta'_x E_A^{2-x}$ , where  $\zeta'_x$  can be determined from the potential. The effect on the range, due to the uncertainty in energy,  $\Delta E$ , at each collision,  $j$ , is

$$(\overline{\Delta R})_j \approx \left( \overline{\Delta E} \frac{ds}{dE} \right)_j$$

where  $s$  is measured along the path of the particle. The accumulated range straggling,  $\overline{\Delta R^2}$ , is

$$\overline{\Delta R^2} = \sum_j (\overline{\Delta R})_j^2 = \sum \left( \overline{\Delta E} \frac{ds}{dE} \right)_j^2$$

where the sum is over all collisions that occur while the particle is stopping. In the CSDA, we have  $\Delta E_j^2 \approx S_{AB}^{(2)} n_B \Delta s_j$ , where  $\Delta s_j$  is the distance between encounters. Hence, replacing the sum by an integral, we have

$$\overline{\Delta R^2} = n_B \int_0^{E_A} S_{AB}^{(2)} \left( \frac{ds}{dE} \right)^2 dE \quad (6.6)$$

which for power laws has the form

$$\overline{\Delta R^2} \approx \frac{\zeta'_x}{2x\zeta_x^3 n_B^2} E_A^{2x} = \frac{E_A S_{AB}^{(2)}}{2x n_B^2 S_{AB}^3} \quad (6.7)$$

The range straggling, like the mean range, is seen to be a monotonically increasing function of energy in each region of  $x$ . To estimate the ion implantation distribution inside of the material, it is often sufficient to write the distribution of stopped particles as a gaussian using  $\bar{R}$  and  $\overline{\Delta R^2}$ , as indicated in Figure 6.3, if the incident particles are not deflected significantly. This is the case when  $M_A \gg M_B$  or when the stopping is primarily due to the electrons.

The mean range,  $\bar{R}$ , is not an easily measurable quantity if the deflections are large. The range provides, however, a measure of the total damage produced in the material. That is, for a low flux of incident particles,  $n_B \bar{\sigma}_D \bar{R}$  is the number of damage sites produced directly by the incident ion, where  $\bar{\sigma}_D$  is an average damage cross section (e.g., breaking a bond, causing an

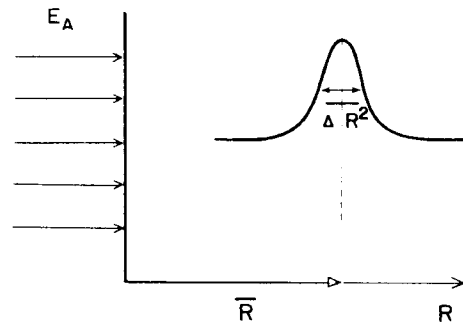


**Figure 6.3.** Schematic diagram of stopped-particle distribution when the deflections are small:  $\bar{R}$  is the mean range and  $\overline{\Delta R^2}$  is the range straggling or root-mean-squared deviation in the range.

ionization, or displacing a target atom). This will be treated in more detail shortly.

For the penetration problem, a more useful quantity is the mean penetration depth,  $\bar{R}_p(E_A)$ , also called the mean projected range and defined in Eq. (6.1). The relationship between  $\bar{R}$  and  $\bar{R}_p$  is indicated schematically in Figure 6.4. Extending the CSDA one would write

$$\bar{R}_p \sim \int_0^{E_A} \frac{\overline{\cos \theta}}{n_B S_{AB}} dE \quad (6.8)$$

where  $\overline{\cos \theta}$  is defined to be an average angle between the incident direction and the direction of motion in the material when the particle has slowed to energy  $E$ . The quantity  $\overline{\cos \theta}$  therefore depends both on  $E_A$  and  $E$ , with  $\overline{\cos \theta}$  decreasing with depth of penetration, i.e. as  $E$  decreases. A useful approximation is to write  $\overline{\cos \theta} \simeq (E/E_A)^{\mu/2}$ , with  $\mu = M_B/M_A$ , where nuclear collisions dominate, and  $\mu \rightarrow m_e/M_A \simeq 0$ , where the energy loss to the electrons dominates. For the power-law cross section Eqs. (6.3) and (6.8) yields the ratio

$$\frac{\bar{R}}{\bar{R}_p} \sim 1 + \frac{\mu}{2x} \quad (6.9)$$

This ratio, the mean range vs the mean projected range, provides a useful estimate of the increase in damage density when the deflections are significant. Remembering that in the approximations used here,  $\mu$  and  $x$  vary slowly in energy, we see that for incident ions the ratio approaches unity at high energies when energy loss to the electrons dominates.

The approximation in Eq. (6.8) for  $\bar{R}_p$ , although useful for indicating the general behavior of this quantity, has limited validity. In the following section the more accurate integral equation method for determining  $\bar{R}$  and  $\bar{R}_p$  is presented. This method incorporates the statistical nature of the stopping process, which is especially important in determining  $\bar{R}_p$ .

## Integral Equations for Range and Projected Range

The mean range and mean projected range of a particle undergoing a series of collisions is obtained by summing the average distances between

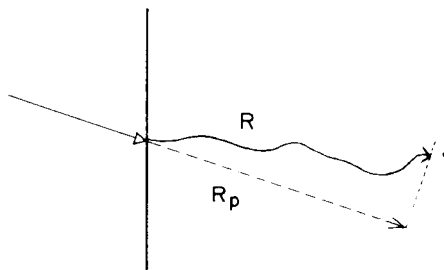


**Figure 6.4.**  $R$ , the range, is total distance traveled by an incident particle, and  $R_p$ , the projected range, is the distance penetrated along the initial direction of motion.

collisions. If the mean free path of the projectile at energy  $E_A$  is

$$\lambda_{AB} = [n_B \sigma_{AB}(E_A)]^{-1}$$

(viz. Chapter 2), the mean range can be written as the mean free path for the first collision plus the mean range of the particle after this collision. As the distance traveled after the first collision depends on the energy loss in that collision, the range is written

$$\bar{R}(E_A) = 1/n_B \sigma_{AB} + \int_0^{\Delta E_{\max}} \bar{R}(E_A - \Delta E) d\sigma_{AB}/\sigma_{AB} \quad (6.10)$$

where  $\Delta E$  accounts for elastic and/or inelastic energy loss. In Eq. (6.10)  $d\sigma_{AB}/\sigma_{AB}$  is the probability of an energy loss  $\Delta E$  occurring in the first collision, where  $d\sigma_{AB} \equiv (d\sigma_{AB}/d\Delta E) d\Delta E$ . After the first collision, the particle has a mean range  $\bar{R}(E_A - \Delta E)$  and the integral implies an average over all possible first collisions. As the particle is moving in a new direction after the first collision, the corresponding equation for  $\bar{R}_p$  is

$$\bar{R}_p(E_A) = 1/(n_B \sigma_{AB}) + \int_0^{\Delta E_{\max}} \bar{R}_p(E_A - \Delta E) \cos \theta_A d\sigma_{AB}/\sigma_{AB} \quad (6.11)$$

where  $\cos \theta_A$  is the deflection angle in Table 2.4 for a given energy loss  $\Delta E$ .

When the cross section  $\sigma_{AB}(E_A)$  is finite, and the collision energy low, Eqs. (6.10) and (6.11) can be solved by iteration. That is,

$$\begin{aligned} \bar{R}(E_A) = & \lambda_{AB}(E_A) + \int_0^{\Delta E_{\max}} \lambda_{AB}(E_A - \Delta E) d\sigma_{AB}/\sigma_{AB} \\ & + \int_0^{\Delta E_{\max}} d\sigma_{AB}/\sigma_{AB}(E_A) \\ & \times \int_0^{\Delta E'_{\max}} \lambda_{AB}(E_A - \Delta E - \Delta E') d\sigma_{AB}/\sigma_{AB}(E_A - \Delta E) + \dots \end{aligned} \quad (6.12)$$

Noting that  $d\sigma_{AB}/\sigma_{AB}$  is the probability of a collision with energy loss between  $\Delta E$  and  $\Delta E + d\Delta E$ , we see that the sum above implicitly represents the total path as a series of collisions separated by mean free paths,  $\lambda_{AB}$ . Although this iterative method is instructive, it is not particularly useful for determining  $\bar{R}$  or  $\bar{R}_p$ , particularly for singular cross sections.

An alternate procedure, which yields analytic solutions for the power-law cross sections, begins with a rearrangement of Eqs. (6.10) and (6.11) in the form

$$1 = n_B \int_0^{\Delta E_{\max}} d\sigma_{AB} [\bar{R}_p(E_A) - \cos \theta_A \bar{R}_p(E_A - \Delta E)] \quad (6.13a)$$

where the equation for  $\bar{R}$  is obtained by replacing  $\cos \theta_A$  by one. In this form, as  $\Delta E \rightarrow 0$  (hence  $\cos \theta_A \rightarrow 1$ ) and  $d\sigma/d\Delta E \rightarrow \infty$ , the two terms in brackets cancel. When small energy transfers dominate, expanding  $\cos \theta_A$  and  $\bar{R}_p(E_A - \Delta E)$  about  $\Delta E = 0$ , we can recover the CSDA expressions in Eqs. (6.3) and (6.8). This emphasizes that for small energy transfers, which is the case when the targets are the atomic electrons, the stopping is like a drag force, and this is the justification for the separation of the electronic energy loss term in the integral equation [Eq. (1.2)], in Chapter 1. It is also common to separate these processes when determining  $\bar{R}_p$ ; that is, one writes

$$1 = n_B \int_0^{\gamma E_A} (d\sigma/dT) dT [\bar{R}_p(E_A) - \cos \theta_A \bar{R}_p(E_A - T)] + n_B S_c [d\bar{R}_p/dE_A] \quad (6.13b)$$

where, as usual,  $T$  is the elastic nuclear energy transfer which produces the deflections.

The general form for the power-law cross section is  $d\sigma/d\Delta E = C_{AB}/(E_A^a \Delta E^{1+b})$ , which yields the expression used earlier,  $S_{AB} = \xi_x E_A^{1-x}$ , when  $x = a + b$  and  $\xi_x = \gamma/(1 - b)$ . (In the Born approximation,  $a = 1$ ,  $b = 2 - n$ ; in the classical impulse approximation,  $a = b = 1/n$ , both for  $V \propto R^{-n}$ .) Substituting this expression into Eq. (6.13a) and writing  $y = \Delta E/E_A$ , we solve this equation in the form  $\bar{R}_p(E_A) = \bar{R}_p^0 E_A^x$ . With  $\Delta E_{\max} = \bar{\gamma} E_A$ , where  $\bar{\gamma}$  is determined by the dominant energy transfer mechanism (i.e., to nuclei or electrons), the constant  $\bar{R}_p^0$  is seen to be

$$(\bar{R}_p^0)^{-1} = n_B C_{AB} \int_0^{\bar{\gamma}} \frac{dy}{y^{1+b}} [1 - (1 - y)^x \cos \theta_A] \quad (6.14)$$

When applying Eq. (6.14) to elastic nuclear-energy transfer,  $\Delta E \rightarrow T$ ,  $\bar{\gamma} = \gamma$ , and, from Eq. (2.41), we have  $\cos \theta_A = \{1 - [(1 + \mu)/2](T/E_A)\} / (1 - T/E_A)^{1/2} = \{1 - [(1 + \mu)/2]y\} / [1 - y]^{1/2}$ .

For simple isotropic scattering of equal mass particles, the cross section can be described using  $b = -1$ ,  $a = 1$ , and  $C_{AB} = \sigma_{AB}$ , in which case  $\bar{R}_p = 3/n_B \sigma_{AB}$ . That is, a superthermal molecule of a gas will move about three mean free paths in the initial direction of motion while slowing down, which the reader should verify, is 3/4 the result obtained using Eq. (6.8). Of course, the total path length,  $\bar{R}$ , is infinite with such a cross section. That is, the particle rattles around a lot before thermalizing, but does not progress very far. The energy dependence obtained from the integral equations does not differ from that obtained in the CSDA; however, the multiplicative constant is different (we leave as an exercise the problem of comparing the

magnitude of the result here to the CSDA for power-law potentials: Problem 6.2.

The general procedure for solving Eq. (6.13), when a more complicated cross section is used or both electronic and nuclear energy loss contribute, is to assume an analytic form for  $\bar{R}_p$ . That is, we write  $\bar{R}_p$  as a sum of terms each having a different energy dependence with variable coefficients. The “best” coefficients are then obtained by minimizing the difference between the left- and right-hand side of the integral equation. The result of such a calculation is given in Figure 6.2. For implantation of ions we would also like to know the range straggling. Rather than calculate this quantity directly, we proceed in the following section to consider equations describing the stopped particle distribution and obtain the straggling as a product.

### Stopped-Particle Distribution

In the last two sections we constructed methods for obtaining two of the parameters which characterize the stopped-particle distribution, that is,  $\bar{R}$  and  $\Delta R^2$ . It would, of course, be preferable to obtain the distribution itself, or at least have a scheme for determining it as accurately as possible.

To describe the distribution of stopped particles another integral equation is constructed. We define  $F(E_A, \hat{p}_A, z)$  to be the number density of stopped particles at depth  $z$  that had initial energy  $E_A$  and direction  $\hat{p}_A$ . This distribution is made up of contributions from particles that had different collision histories as they come to a stop. Following Chartres, Lindhard, Sigmund, and others we consider the collisions occurring in the first layer of material. From Figure 6.5 it is clear that the distribution,  $F(E_A, \hat{p}_A, z)$ , at a depth  $z > \Delta z$  determined by the flux of particles starting at  $z = 0$  is equivalent to the distribution determined by the flux of particles emerging at  $\Delta z$ . Some of these particles have a collision in the layer and emerge with a new energy and direction. Recalling that  $(\Delta z n_B / \hat{p}_A \cdot \hat{z}) d\sigma_{AB}$  is the probability of a collision occurring in the layer resulting in an energy loss between  $\Delta E$  and

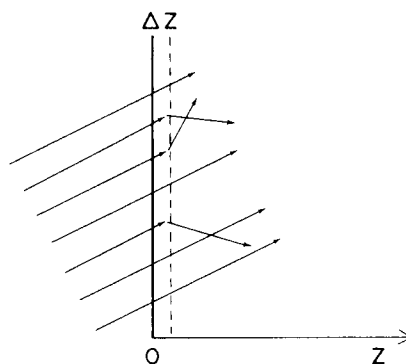


**Figure 6.5.** Change in the incident-particle flux after passing through a layer  $\Delta z$  thick.

$\Delta E + d\Delta E$ , we obtain the distribution at  $z > \Delta z$ :

$$F(E_A, \hat{p}_A, z) = (\Delta z n_B / \hat{p}_A \cdot \hat{z}) \int d\sigma_{AB} F(E_A - \Delta E, \hat{p}'_A, z - \Delta z) \\ + [(1 - \Delta z n_B \sigma_{AB}) / \hat{p}_A \hat{z}] F(E_A, \hat{p}_A, z - \Delta z)$$

The first term on the right accounts for those particles scattered in the layer, and the second for those emerging without a scattering. The quantity  $F(E_A - \Delta E, \hat{p}'_A, z - \Delta z)$  is the stopped-particle distribution at  $z$  for particles starting at  $\Delta z$  with energy  $E_A - \Delta E$  and momentum  $\hat{p}'_A$ . Rearranging terms and letting  $\Delta z \rightarrow 0$ , we obtain the integral equation

$$-\cos \theta \frac{\partial}{\partial z} F(E_A, \hat{p}_A, z) = n_B \int d\sigma_{AB} [F(E_A, \hat{p}_A, z) - F(E_A - \Delta E, \hat{p}'_A, z)] \quad (6.15)$$

where  $\cos \theta \equiv \hat{p}_A \cdot \hat{z}$ .

It is customary to separate electronic and nuclear energy transfers as in Eq. (1.2), giving the following integral-differential equation for  $F$ :

$$-\cos \theta \frac{\partial}{\partial z} F(E_A, \hat{p}_A, z) = n_B \int_0^{E_A} \frac{d\sigma}{dT} [F(E_A, \hat{p}_A, z) - F(E_A - T, \hat{p}'_A, z)] dT \\ + n_B S_e \frac{\partial}{\partial E_A} F(E_A, \hat{p}_A, z) \quad (6.16)$$

Although the equation is similar in form to Eq. (1.2), the quantities to be determined,  $F$  and  $I$ , have different boundary conditions. On comparing these equations, we see that the probability per unit pathlength of a momentum change, postulated in Eq. (1.2), has the form (see also Appendix E)

$$\omega(\mathbf{p}, \mathbf{p}') d^3 p' = n_B \left( \frac{d\sigma}{dT} \right) dT \delta[\hat{p}' - \hat{p}(T)] d\hat{p}' \quad (6.17)$$

and the integral over  $d\hat{p}'$  has been carried out in Eq. (6.16). The delta function arises from the classical collision kinematics of Chapter 2 as each  $T$  corresponds to a particular direction change.

Before examining the distribution in detail it is worth noting that if  $M_A \gg M_B$ , so that  $T$  and the scattering angle  $\hat{p}_A \cdot \hat{p}'$  are small, then Eq. (6.16) reduces to

$$-\cos \theta \frac{\partial}{\partial z} F \sim n_B (S_e + S_n) \frac{\partial}{\partial E_A} F \quad (6.18a)$$

Now depth and energy are simply related and all the particles stop at the same point, producing a delta-function distribution. This is simply the continuous slowing-down approximation. In the opposite extreme, if each collision leads to an absorption of an incident particle (stopping), then from

Eq. (6.15) we have

$$F \sim F_0 \exp[-n_B \sigma_{AB} z / \cos \theta] \quad (6.18b)$$

where  $F_0$  is a normalization constant,  $n_B$  is assumed constant, and the  $\cos \theta$  allows for other than perpendicular incidence. This is the situation when incident light or slow neutrons are absorbed by a material. In fact this distribution is not unlike that for slow, heavy atoms which lose their forward motion in a couple of collisions. In the following the more general case is considered.

As Eq. (6.16) is very difficult to solve, the distribution is often expressed by its moments

$$F^n(E_A, \hat{p}_A) = \int_{-\infty}^{\infty} z^n F(E_A, \hat{p}_A, z) dz \quad (6.19)$$

The zeroth moment, which is the total number of stopped particles, provides one condition on the solution. For sufficiently thick targets, all particles are stopped unless they are backscattered from the material. Normalizing  $F$  to be the probability distribution per incident particle, we have

$$\langle z^0 \rangle \equiv F^0 = 1 - \text{probability of backscattering} \quad (6.20)$$

In many examples the backscattering probability is small, in which case  $F^0 = 1$ . The mean projected range is simply related to  $F^1$ , i.e.,  $\langle z \rangle \equiv \bar{R}_p(E_A) \cos \theta = F^1 / F^0$ , and the projected range straggling is  $\langle \Delta z^2 \rangle \equiv \langle (z - \langle z \rangle)^2 \rangle = (F^2 - \langle z \rangle^2) / F^0$ .

The simplest approximation to  $F(E_A, \hat{p}_A, z)$  is a gaussian, as in Figure 6.3, using  $\langle z^0 \rangle$ ,  $\langle z \rangle$ , and  $\langle \Delta z^2 \rangle$ ,

$$F(E_A, \hat{p}_A, z) \approx \frac{\langle z^0 \rangle}{[2\pi \langle \Delta z^2 \rangle]^{1/2}} \exp\left[-\frac{(z - \langle z \rangle)^2}{2\langle \Delta z^2 \rangle}\right] \quad (6.21)$$

which involves determining  $F^0$ ,  $F^1$ , and  $F^2$ . Integral equations for these quantities are obtained by multiplying Eq. (6.15) by  $z^n$ , integrating and using Eq. (6.19). Applying this procedure, we find that the equation for  $F^1$  is equivalent to that for  $\bar{R}_p$ , Eq. (6.13a), when the simple angular dependence associated with the incident particle direction is removed. The angular dependence in the higher terms,  $F^n$ , is generally expressed using the Legendre polynomials  $P_l(\cos \theta)$ . Noting that  $z$  very nearly scales as  $\cos \theta$ , one can write  $F^n(E_A, \hat{p}_A) = \sum_l P_l(\cos \theta) F_l^n(E_A)$ , where  $l \leq n$  and  $l$  is odd for  $n$  odd, even for  $n$  even. Winterbon and others have constructed codes for determining the moments,  $F_l^n$ , for simple cross sections. These are then used to reconstruct the distribution, with the gaussian distribution in Eq. (6.21) being the simplest form. When moments higher than  $F^2$  are used, a number of reconstruction methods may be employed, which lends a certain arbitrariness to the result. However, comparisons of reconstructed (from moments) distributions and simulation calculations generally show reasonable agreement, except near  $z = 0$ .

The stopped-particle or projected range distribution for normal incidence is shown in Figure 6.6 for 1-keV protons entering a biological-like target. The moments were obtained using the Lindhard–Thomas–Fermi approximation to  $d\sigma/dT$  discussed in Appendix H and the Lindhard–Scharff low-energy stopping formula [Eq. (5.31)]. The range distribution is seen to be skewed only slightly for this case, although this is clearly not typical of all distributions or combinations of projectile and target, e.g., the extreme case is the solution (6.18b). When  $M_A$  is large compared to the target mass the width of the distribution narrows, approaching a delta function in the limit where the CSDA is valid, the solution to (6.18a). In these examples the material is treated as infinite and  $F^0 = 1$ .

### Diffusion of Implanted Particles, Backscattering, and Transmissions

The gaussian form for  $F$  in Eq. (6.21), although approximate, provides a useful initial condition for describing the diffusion of the stopped particles. These particles are said to be stopped in the sense that they have attained temperature equilibration with the target material. However, as the distribution of these particles is nonuniform, thermal diffusion will occur. The “stopped”, and by now neutralized, particle will migrate until it leaves the material, reacts with a material component, or is trapped (at a lattice or interstitial sight, or in a physical gap or hole in the material).

The diffusion-reaction process is described by the rate equations developed in Chapter 1. That is, in a uniform material, the particle distribution  $F(\mathbf{r}, t)$  is determined from

$$\frac{\partial}{\partial t} F(\mathbf{r}, t) = +D(T)\nabla^2 F(\mathbf{r}, t) - v_R(T)F(\mathbf{r}, t), \quad (6.22)$$

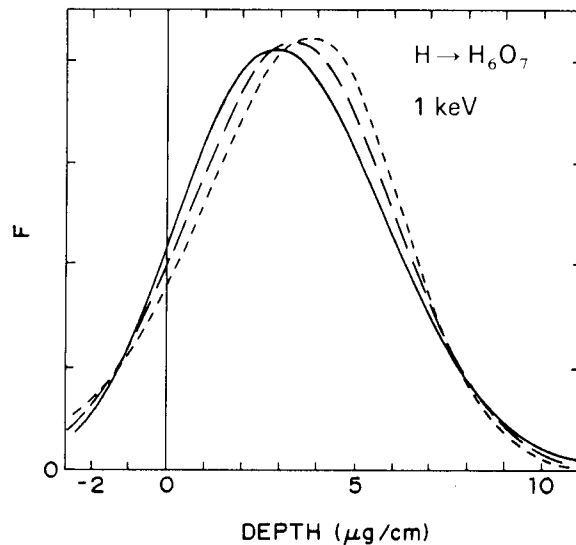


**Figure 6.6.** Stopped-particle distribution,  $F$ , for  $H \rightarrow H_6O_7$  (target: RNase-like weighting of light and heavy atoms): short-dashed line, using three moments; long-dashed line, using four moments, solid line, using five moments. [From R. Romanelli, Ph.D. thesis, University of Virginia (1980).]

where the diffusion coefficient,  $D(T)$ , and the reaction frequency,  $\nu_R(T)$ , both depend on the temperature of the material and the species involved. In Chapter 5 the diffusion coefficient for a gas was found to have a temperature dependence,  $D \propto T^{x+1/2}$  for power laws. In a solid, the movement of atoms (or vacancies) between sites occurs in jumps. Because an energy barrier exists for jumping between sites, the diffusion coefficient for a particle in a solid has a form like the Arrhenius reaction rate in Eq. (5.36). That is,  $D(T) = f(T) \exp[-\Delta E_a/kT]$ , where  $\Delta E_a$  is the activation for a jump between sites, and  $f(T)$  is slowly varying with  $D(T)$  approaching the gaseous diffusion limit at high temperatures or small  $\Delta E_a$ .

As  $D$  and  $\nu_R$  are assumed to be independent of depth, Eq. (6.22) has a simple solution when the initial spatial distribution is gaussian. In the one-dimensional problem we have been solving, the distribution of unattached "stopped" particles is

$$F(z, t) = \frac{\langle z^0 \rangle}{[2\pi\langle \Delta z^2 \rangle_t]^{1/2}} \exp \left[ -\frac{(z - \langle z \rangle_0)^2}{2\langle z^2 \rangle_t} \right] \exp(-\nu_R t) \quad (6.23)$$

where  $\langle z^0 \rangle$  is  $F^0$  of Eq. (6.18) and the subscripts indicate the time dependence. In this expression  $\langle z \rangle_0 = \langle z \rangle$ , the stopped-particle mean penetration depth of the previous section, and  $\langle \Delta z^2 \rangle_t = \langle \Delta z^2 \rangle + 2D(T)t$ , so that Eq. (6.23) reduces to Eq. (6.20) as  $t \rightarrow 0$ . A quantity of greater interest in ion implantation is the distribution of bounded or trapped, implanted particles at  $t \rightarrow \infty$ , (Problem 6.12).

A fraction of an ion beam is backscattered from surface or interior atoms. This fraction increases with decreasing ion velocity and in Figure 6.6 is the part of the distribution to the left of the surface. Of interest for material analysis are those backscattered particles having experienced a single, hard collision. For fast, light ions ( $\approx 1$  meV/amu) the reflections are a result of close ( $b \simeq 0$ ) Coulomb collisions with the nuclei of the target atoms, [Eq. (2.61b) with  $n = 1$ ,  $T = \gamma E_A$ ]. The total energy loss of such backscattered particles is roughly  $\gamma E_A + n_B S_e(2\bar{z})$ , where  $\bar{z}$  is the depth at which the collision occurred. As  $\gamma$  depends on the mass of the target atom and  $S_e$  is tabulated, measuring the energies of the particles backscattered can provide a depth distribution for near surface impurity atoms or the thicknesses of thin films deposited on a known substrate.

The number of particles transmitted through a foil can be calculated by extensions of the techniques discussed above. In Figure 5.6 such particles were used to estimate the interaction potential with target atoms. Transmission experiments are also used to determine spectra of ions and structures of molecular ions. As fast ions are further ionized (stripped) and excited on transmission through thin carbon foils, the electronic relaxation processes are monitored after the ions exit the foil. Highly stripped molecules, for instance, will "explode" due to the Coulomb repulsion between

the nuclei. Although, this repulsive energy,  $Q_r$ , is a small fraction of the incident kinetic energy,  $E_A$ , in the laboratory frame (Table 2.3), significant changes in kinetic energies of the fragments ( $\sim(Q_r E_A)^{1/2}$ ) are observed if the repulsive force is nearly parallel to the incident velocity. Knowing the charge states produced by stripping and monitoring the exiting-ion energies and angles due to the repulsion, initial bond lengths and dissociation energies can be deduced for simple molecular ions which may be difficult to examine spectroscopically.

### Energy Deposition Effects

The previous sections have dealt with the behavior of the incident particles and not the description of the alterations produced in the target material by incident radiation. Alterations, such as net ionization or number of displaced particles, are often characterized by the energy deposition per unit volume, or for uniformly irradiated materials, the energy deposited per unit pathlength.

Using the CSDA and power laws, the penetration distance and particle energy can be simply related. Neglecting deflections, the penetration depth,  $z$ , at which the incident particles have been slowed to an average energy  $\bar{E}$  is

$$z \sim \int_{\bar{E}}^{E_A} (1/n_B S_{AB}) dE \quad (6.24)$$

Employing the simple approximation for  $S_{AB}$  that we have been using and Eq. (6.4), we reduce Eq. (6.24) to the form  $z \sim \bar{R}_p - \bar{E}^x / (x \xi_x n_B)$ . We can now estimate the general form for the energy deposition rate at any depth  $z$  using  $\bar{E}$  from Eq. (6.24) and Eq. (6.2) for the energy loss rate,

$$-dE/dz \sim (n_B \xi_x)^{1/x} [x(\bar{R}_p - z)]^{1-1/x} \quad (6.25)$$

For slow collisions in the electronic stopping regime where  $x \sim \frac{1}{2}$ , the energy deposition decreases slowly with depth, whereas for fast collisions (i.e.,  $1 < x < 2$ ), it is strongly peaked toward the end of the path. This is seen in Figure 6.7 for fast heavy particles on tissue-equivalent material, which yields the typical Bragg curve for energy deposition. The localized, high-density radiation deposited at the end of the path is something one tries to exploit when using ion beams to selectively irradiate targets in a material. That is, one would guess that for fast particles the major damage to the material occurs at the end of the path, where, of course, the deposited particles are also found. In slow collisions for which elastic nuclear energy loss is important, the deposited energy distribution is obtained from an integral equation and resembles the range distribution in form (viz. Figure 6.6).

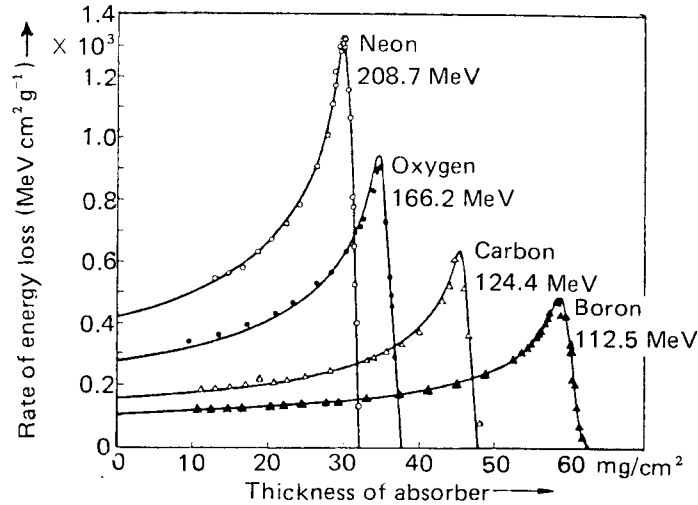


**Figure 6.7.** Bragg curves for heavy ions in tissue-equivalent material (use  $\rho \approx 1 \text{ g/cm}^3$  for density conversion). [From T. Brustad, *Radiat. Res.* **15**, 139 (1961).]

Damage to a material may be associated with a number of changes induced by the incident particles. One measure of damage is the number of target atoms displaced from their original site. Such damage may be repaired by diffusion processes, but this discussion will concentrate on the initial damage produced. Dividing the amount of energy deposited in *elastic* collisions by twice the energy required to displace a target atom in a dynamic collision has been shown to give a reasonable estimate of the number of displaced atoms. This model, based on the Kitchin–Pease approximation for solving the integral equations, is widely used for estimating displacement damage. The corresponding concept in ionization production has been extensively verified. That is, over a broad range of energies, where  $S_e \gg S_n$ , the average energy deposited per ionization produced is a constant, which we write as  $W_e$ . This number, referred to as the  $W$  value, is roughly related to the ionization potential (i.e., the energy required to displace an electron), as indicated for a few targets in Table 6.1. If the total energy  $E$  is separated into that part deposited elastically,  $v$ , and that deposited inelastically,  $\eta$  (i.e.,  $E_A = v + \eta$ ), the number of ionizations is  $\eta/W_e$  and the number of displacements is  $v/W_n$ , where  $W_n$  is approximately twice the displacement energy. (It is traditional to use  $v$  for the elastic energy deposited and  $\eta$  for the electronic energy, and the reader should not confuse these with a collision frequency or a phase shift.)

Based on the above notions, a rough approximation to the number density of displaced particles at various depths is

$$n_D(z) \simeq \phi_A n_B S_n(\bar{E})/W_n \quad (6.26)$$

with  $\bar{E}(z)$  determined from Eq. (6.24). Equation (6.26) applies only for small fluences  $\phi_A$ ;  $\phi_A$  is the particle flux (assumed perpendicular and uniform)

**Table 6.1.**  $W$  Values at High Energies: Average Energy Required to Produce an Ion Pair for a Particle Stopping in a Gas

Target	$I^b$	$W_e(\text{H}^+)$	$W_e(\text{He}^{++})$	$\sim W_e/I$
He	24.5	45.	44.	1.8
Ne	21.6	39.	36.8	1.8
Ar	15.8	26.6	26.3	1.7
Kr	14.0	23.0	24.1	1.7
Xe	12.1	21.	21.6	1.8
N <sub>2</sub>	15.6	37.	36.4	2.4
Air <sup>c</sup>	14.9	35.2	35.1	2.4
CO <sub>2</sub>	13.8	34.4	34.2	2.5
TE <sup>d</sup>	13.1	30.	31.	2.3
CH <sub>4</sub>	12.6	31.	29.	2.4

<sup>a</sup> H. Bischel, D. H. Pearson, J. W. Boring, A. Green, M. Inokuti, and G. Hurst, ICRU Report No. 31, Washington, D.C. (1979).

<sup>b</sup>  $I$  is the first ionization potential.

<sup>c</sup>  $I$  based on average mixture of N<sub>2</sub>, O<sub>2</sub>, and Ar.

<sup>d</sup> TE is tissue-equivalent gas: 64.4% CH<sub>4</sub>, 32.4% CO<sub>2</sub>, and 3.2% N<sub>2</sub>.

times the exposure time. For fast collisions, as the mean energy  $\bar{E}$  is determined by the electronic stopping power and  $S_n$  increases with decreasing energy,  $n_D(z)$  is also peaked near the end of the path. In this example it is assumed that all the energy deposited by the incident particle in elastic collisions goes into nuclear motion. However, the fast secondaries produced in these collisions may in fact lose a considerable fraction of their energy inelastically and will deposit their energy away from the initial collision site. The integral equation approach will correct both of these oversights. Here we use the fact that the production of slow secondaries dominates. As these particles lose *most* of their energy elastically (i.e.,  $v(E) \rightarrow E$  as  $E \rightarrow 0$ ), and do not travel far from the initial production point, a first-order improvement to the result in Eq. (6.26) is

$$n_D(z) \sim \frac{\phi_A n_B}{W_n} \int_0^{\gamma \bar{E}(z)} v(T) \frac{d\sigma}{dT} dT \quad (6.27)$$

with  $v(T) \sim \int_0^T [S_n/(S_e + S_n)] dE$ . The reader should note that these "simple" methods rapidly become complex and the approximations made rather restrictive. The integral equation method, which at first sight seems rather involved, begins to appear more attractive as the accuracy required increases. Equations (6.26) and (6.27) can both be integrated to yield the total number of displacements produced per incident particle  $v/W_n$ .

A useful quantity, related to the displacement problem, is the number of recoils with energy between  $T$  and  $T + dT$  produced at any depth in a

cascade initiated by a particle of energy  $E_A$  which we write  $G(E_A, T)$ . Solving the collision cascade equation, which includes all recoils, Sigmund has shown that

$$G(E_A, T) \sim \beta_n \frac{v(E_A)}{T^2} \quad \text{for } E_A \gg T \quad (6.28)$$

where  $n$  labels the power law used to describe collisions of the secondaries with atoms of the target material. Using an exponential potential ( $n \rightarrow \infty$ ) to describe the slow elastic collisions, we have  $\beta_0 = 6/\pi^2$  in Eq. (6.28). The number of displacements per incident ion is found by integrating Eq. (6.28) over all energies greater than the displacement energy,  $E_D$ . This procedure yields the result

$$\int_{E_D}^E G(E_A, T) dT \sim \frac{6}{\pi^2} \frac{v(E_A)}{E_D} \quad (6.29)$$

implying  $W_n \sim 1.64E_D$ . Accounting for replacement collisions which occur when the incident-particle's energy is less than  $E_D$  after the collision, one finds that  $W_n \sim 2.4E_D$ . These results are both close to the Kitchin–Pease result,  $W_n \sim 2E_D$ , assumed earlier.

In the following section we extend these ideas to consider, first, damage to a biological sample and, then, the amount of target material removed by an incident ion, or the sputtering of the target.

## Biological Damage

Simple enzymes, involving a single, long chain of molecules (strand), folded by hydrogen bonds, are known to be damaged by a single “hit” from incident, heavy-particle radiation. Defining exactly what constitutes a “hit” is rather difficult, however. It appears that radicals such as  $\text{OH}^-$ ,  $\text{H}_3\text{O}^+$  and electrons in an aqueous solution are very effective in damaging biological molecules. These radicals are products of the ionization and dissociation of  $\text{H}_2\text{O}$  by the incident radiation. The radicals apparently diffuse to a sensitive site of the enzyme and react destructively. This type of damage, referred to as indirect, is controlled to a large extent by diffusion and chemistry occurring after the initial energy deposition. For comparison, samples are often freeze-dried to remove the water content, so the direct effect of the radiation can be measured. Although a considerable body of knowledge has accumulated regarding the chemical kinetics that follow the initial energy deposition events, obtained using ingenious experimental procedures, this discussion will deal with initial events only.

If a material is irradiated for a time,  $t$ , it was shown in Chapter 2 that the probability of a given target, within the material, receiving a hit in-

creases exponentially. Conversely the survival probability is, based on Eq. (2.12), the simple Poisson distribution function

$$P_S = \exp[-\sigma_h \phi_A] \quad (6.30)$$

where  $\Phi_A$  is the fluence ( $\phi_A = It$ ) and  $\sigma_h$  is the hit cross section. We note in passing, that in double-stranded material (e.g., DNA) it is thought that two separate hits, presumably one on each strand, are required for damage, in which case

$$P_S = 1 - (1 - \exp[-\sigma_h \Phi_A])^2 \quad (6.31)$$

which has a different dependence on fluence, as indicated schematically in Figure 6.8. In the following an expression for  $\sigma_h$  is constructed.

We define  $F_D(z, r, E_A)$  to be the number density of damage sites produced in a biological material (consisting of a large number of enzymes, either freeze dried or in an aqueous solution) by an incident ion of energy  $E_A$ . These damage sites may be produced directly by ionization and dissociation, or indirectly by diffusing radicals resulting from ionization and dissociation events. In the quantity  $F_D(z, r, E_A)$ ,  $r$  indicates the radial distance from the incident particle direction (presumed normal to the surface for simplicity), and  $z$  the depth into the bulk material. Such a quantity is calculated from the integral equation describing the cascade (or the CSDA) and subsequent diffusion kinetics, as in the previous examples. Since the fast secondary electrons produced, often called delta rays, can travel quite far before stopping and, in addition, diffusion acts to distribute the product radicals, damage may take place at significant distances, on a molecular scale, from the initial track. If the energy deposited per unit path length by the incident particle is large, then the damage has roughly a uniform, cylindrically symmetric distribution about the incident particle track. Using a power cross section in the Born approximation for the production of ioni-

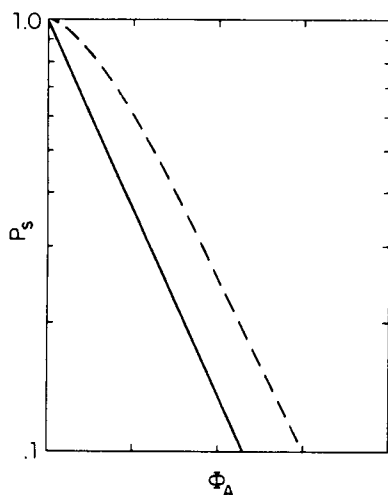


**Figure 6.8.** Survival probability,  $P_S$ , vs. fluence,  $\Phi_A$  (flux  $\times$  time): solid line, single-hit targets; dashed line, double-hit targets.

zation, we leave it to the reader (Problem 6.15) to show that the distribution of the inelastic energy deposited by a fast primary is

$$\left(\frac{dE}{dV}\right)_e \sim \frac{1}{2\pi R_{\max}^2} \left|\frac{dE}{ds}\right|_e \left(\frac{n-1}{2-n}\right) \left(\frac{R_{\max}}{r}\right)^{3-n} \left[1 - \left(\frac{r}{R_{\max}}\right)^{2-n}\right] \quad (6.32)$$

for  $1 < n < 2$ . In Eq. (6.32) it was assumed, for simplicity, that the secondary electrons lose energy at a constant rate and move perpendicular to the track, with  $R_{\max}$  the maximum range for the electrons. As  $F_D(z, r, E_A)$ , according to the previous discussion, is simply related to  $(dE/dV)_e$ , the damage distribution is seen to be peaked close to the track and decreases slowly with distance from the track. The experimental results for deposited dose in a gas shown in Figure 6.9 indicate the behavior expected from Eq.

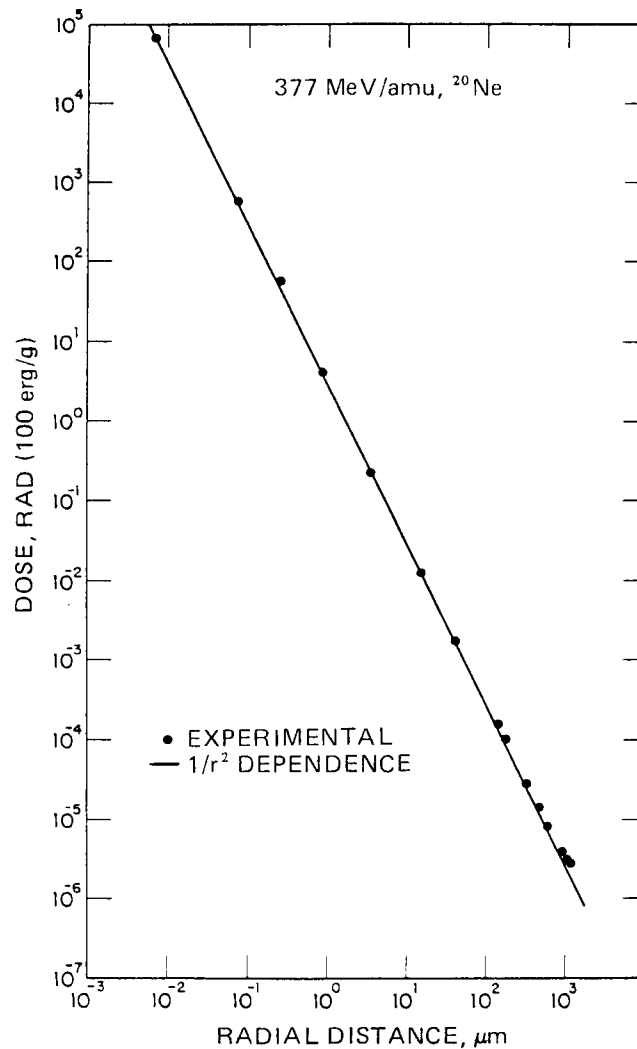


**Figure 6.9.** Dose deposited  $(dE/dV)_e$  in a tissue-equivalent gas versus radial distance from incident Ne direction. Distance scale based on an assumed density of  $1 \text{ g/cm}^3$ . [From: M. N. Varma and J. W. Baum, *Radiat. Res.*, **81** 335 (1980)].

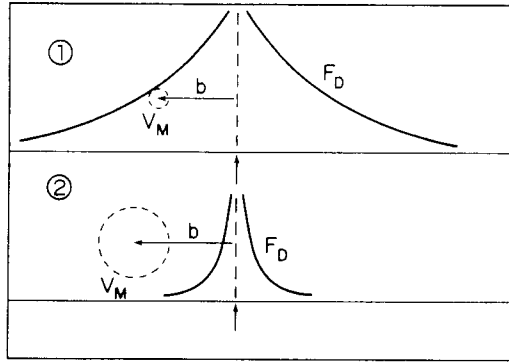


**Figure 6.10.** Examples of target,  $V_M$ , damaged by passing particle: case 1, dimensions of target small; case 2, target dimensions large compared to spread in energy density.

(6.32). For very low energy-density radiations, effects produced by the individual secondary electrons do not overlap, a tacit assumption in obtaining a continuous distribution like that in Eq. (6.32). If each fast secondary produces a separate damage cascade or spur off the primary particle track, then  $(dE/dV)_e$  or  $F_D$  only defines the average distribution of events. A more careful treatment would consider the size and distribution of energy deposited within the cascades, and the random distribution of the cascades. The two limits, separate and overlapping cascades, will be considered more carefully in the next section when discussing sputtering.

In constructing the damage cross section, attention has to be paid to the fact that even simple biological systems, like enzymes, have more than one sensitive site. That is, damage can be incurred by “hitting” any one of a number of “targets.” Calling the volume of the biological molecule (here an enzyme)  $V_M$ , the *average* number of damages,  $\eta_D(z, b, E)$ , produced by *one* incident particle in an enzyme centered a distance  $b$  from the incident direction is obtained by integrating  $F_D$  over the volume of the enzyme,  $\eta_D \sim \int_{V_M} F_D dV$ . Consider the two cases shown in Figure 6.10. In case 1, the dimensions of the molecules are small compared to the extent of  $F_D$  and, therefore,  $\eta_D \sim V_M F_D(z, r, E_A)$ . In the opposite limit,  $V_M$  is large (or  $F_D$  narrowly distributed), in which case either the particle misses ( $b > L_M/2$ ,  $L_M \sim$  linear dimensions of a molecule) and  $\eta_D \sim 0$ , or it passes through the molecule ( $b < L_M/2$ ) and  $\eta_D \sim L_M F_D(z, E)$ . Here,  $F_D(z, E)$  is the damage deposited per unit path length [ $F_D(z, r, E)$  integrated over the radial dimensions], a quantity we described in the previous section. As an enzyme has a number of sensitive sites, the *average* number of damages in  $V_M$  may be greater than one. Using this average, we see that the Poisson probability for the occurrences of *at least* one damage in  $V_M$ , initiated by a particle passing at a distance  $b$  away, is

$$P_D(z, b, E_A) = 1 - \exp[-\eta_D(z, b, E_A)] \quad (6.33)$$

and  $P_D$  is seen to be less than one no matter how large  $\eta_D$  is. This fact—one molecule can only be counted as one damaged molecule—is often referred

to as saturation when the damage density, hence  $\eta_D$ , is large. For low damage density when  $\eta_D$  is small, which is often the case at distances away from the incident particle path,  $P_D \approx \eta_D$ .

By what may appear to have been a sleight of hand, we have constructed an impact-parameter probability for producing an effect (here damage) in a multiple-target molecule. Now the cross section for the effect is constructed as always [viz. Eq. (2.24)]

$$\sigma_D = 2\pi \int_0^\infty b db P_D(z, b, E) \quad (6.34)$$

In the limit that the molecule has only one target, Eqs. (6.34) and (6.33) reduce to our previous definitions of cross section. The above discussion merely generalizes the concept of cross section, defining it for complex molecular systems. For instance, in calculating the ionization cross section for a large molecule or a molecular cluster such saturation effects have to be included. (The reader should note that binary encounter calculations, in which the probability of producing an effect in each component is summed, apply only if these probabilities are small and hence may grossly overestimate inelastic cross sections (viz. Figure 5.26). The quantity  $\sigma_D$  in Eq. (6.34) can now be used for the "hit" cross section in Eq. (6.30) when describing the survival probability of a colony of enzymes.

For case 2 in Figure 6.10, the damage cross section in Eq. (6.34) becomes

$$\sigma_D \sim \sigma_g \{1 - \exp[-L_M F_D(z, E)]\} \quad (6.35)$$

where  $\sigma_g$  is the average geometric cross-sectional area of the enzyme ( $\sigma_g \approx L_M^2$ ). For high-damage-density radiation in a large target volume Eq. (6.35) yields  $\sigma_D \sim \sigma_g$ , i.e., either the particle passes through the target, damaging it with unit efficiency, or not. For low-damage-density radiation ( $\eta_D \ll 1$ ) both cases 1 and case 2 yield

$$\sigma_D \sim V_M F_D(z, E) \quad (6.36)$$

where  $V_M \sim L_M \sigma_g$ . This is a frequently used approximation for  $\sigma_D$ . Combining Eq. (6.36) with the fact that the damage density  $F_D$  scales like the stopping power [Eq. (6.3.2)] or in the radiation damage literature as LET (a part of  $|dE/ds|$ ), we have  $\sigma_D \propto |dE/ds|$ . Using plots of active fraction versus fluence (Figure 6.8) for thin targets,  $z \sim 0$  in Eq. (6.34), we can obtain damage cross sections. In Figure 6.11 the measured damage cross section for various incident particle radiations on a number of enzymes is seen to depend nearly linearly on the stopping power, confirming this description.

The reader may be surprised by the fact that the damage cross section is many times the geometric cross section at high LET. The derivation of Eq. (6.36) (giving  $\sigma_D$  as proportional to  $F_D$ ) was obtained assuming the



Applying the results of the previous section, in the simple CSDA, we have

$$\sigma_D \sim V_M n_B [(S_e/w_E) + (S_n/w_n)] \quad (6.37)$$

where  $w_n$  and  $w_e$  are the energies deposited per displacement and ionization, respectively, which lead to a biological damage. From Figure 6.11  $w_e$  is found to be about 60 eV in the energy region shown, i.e.,  $S_e \gg S_n$ . For every 60 eV of inelastic energy deposited (roughly twice the  $W$  value for ionization), an average of one damage site is produced in an enzyme. The situation for displacement damage to enzymes is not clear at present; however, in the limit of small fluence the total number of damages produced has the same form as Eq. (6.26). The problem considered in the subsequent section is again related to energy deposition in a material, but the damage effect is a surface effect—the removal or sputtering of atoms from the surface of the target.

## Sputtering

A result of considerable interest related to the displacement of target particles is the sputtering of the surface material by incident ions. Material is ejected by recoil cascades occurring close to the target surface. When the density of recoils is small enough that the secondary particle cascades produced in the target all decay in energy independently, then the flux of particles leaving the surface can be treated in a straightforward manner. The sputtering yield,  $Y$ , is defined to be the number of material particles exiting the target per incident particle. This yield consists of contributions from all cascades produced near the surface, each cascade associated with a secondary particle produced by the incident ion. For simplicity, we assume the cascades are spherically symmetric spurs about the ion's path located at random distances from the surface. From each cascade (hot spot) the collision energy moves outward, eventually transporting atoms across the target surface.

Using these ideas, we construct the sputtering yield as follows. Defining  $S_p(z, \Delta E)$  to be the sputtering from a cascade at depth  $z$ , due to the deposition of energy  $\Delta E$ , and  $(n_B d\sigma_{AB})$  to be the number of cascades of energy  $\Delta E$  produced per unit path length, we obtain the total yield

$$Y = n_B \int_0^{\bar{\gamma}E_A} d\sigma_{AB} \int_0^\infty Y(z, \Delta E) dz \quad (6.38)$$

where  $\Delta E$  is  $T$  or  $Q$  depending on whether the source of sputtering is nuclear or electronic energy deposition. To construct the sputtering contribution from each cascade we need to know the energy distribution of particles in the cascade. Any recoil atom B will have an energy  $E'$  for a time

$\nu_B^{-1}$ , where  $\nu_B$  is the collision frequency. Therefore, the secondary-particle energy spectrum at any time, in those cascades initiated by an event  $\Delta E$ , is determined from the recoil spectrum,  $G$ , discussed earlier [Eq. (6.28)],

$$f(\Delta E, E') \simeq (\psi/\nu_B)G(\Delta E, E')$$

where  $\psi$  is the number of such cascades produced per unit time.

Generally one assumes a sputtering occurs if a recoil particle is produced at the surface or reaches the surface with its perpendicular component of velocity large enough to overcome a potential barrier,  $U_0$ ; that is  $E' \cos^2 \theta' > U_0$ , where  $\theta'$  is the direction of motion of the recoil measured from the normal to the surface. Noting that the cascades are randomly distributed and the velocities randomly oriented, we see that those particles with energy  $E'$  at a depth  $v' \cos \theta'/\nu_B$  with  $\cos \theta' > (U_0/E')^{1/2}$  will be able to exit the material. As  $G(\Delta E, E')$  is the number of particles of energy  $E'$  in the cascade, the first integral in Eq. (6.38) becomes

$$\begin{aligned} \bar{z}(\Delta E) &\equiv \int_0^\infty Y(z, \Delta E) dz \\ &= \frac{1}{2} \int_0^{\Delta E} dE' \int_{(U_0/E')^{1/2}}^1 d \cos \theta' (v' \cos \theta'/\nu_B) G(\Delta E, E') \end{aligned} \quad (6.39)$$

which is a mean sputtering depth for the cascade,  $\Delta E$ . It was assumed in Eq. (6.39) that the positive direction is out of the material when defining the angular limits. Writing the collision frequency as  $\nu_B = n_B \bar{\sigma} v'$  and using Eq. (6.28b), one finds

$$\bar{z} \sim \frac{3}{4\pi^2} \frac{v(\Delta E)}{n_B \bar{\sigma} U_0} \quad (6.40)$$

where it is assumed that  $\sigma$  is energy independent, a condition valid for low-energy recoils and from Eq. (5.5)  $\sigma \simeq \bar{\sigma}_d/2$  as particles have the same mass. Substituting Eq. (6.40) into Eq. (6.38), we obtain the net sputtering yield

$$Y \sim \frac{3}{4\pi^2} \frac{1}{\bar{\sigma} U_0} \int_0^{\bar{\gamma} E_A} v(\Delta E) d\sigma_{AB} \quad (6.41)$$

For  $\Delta E \rightarrow T$ , Eq. (6.41) is the general form obtained by Sigmund from the transport equations for sputtering, and  $\bar{\sigma} \sim 1.8 \text{ \AA}^2$  is used for many atomic materials. Approximating the integral in Eq. (6.41) by  $S_n$ , we have  $Y \sim (0.042/U \text{ \AA}^2) S_n$ . A frequently used result for estimating sputtering due to collision cascades based on the above is  $Y \sim (0.042/U_0 \text{ \AA}^2) \alpha S_n$ , where  $\alpha$  is a factor which accounts for the geometry of the cascade near the surface, the angle of incidence, and the effect of inelastic energy loss in Eq. (6.41). In the keV region  $\alpha$  varies from about 0.2 for incident heavy atoms to about 1 for  $M_B \gg M_A$  and at high energies it approaches 0.5. As  $\alpha$  depends on the mass

of the target atoms, in alloys preferential removal of one atomic species may occur, changing the character of the surface layer. The above expressions are valid when the cascades can be considered to be noninteracting and when  $\Delta E \gg E'$ , as required in Eq. (6.28). For molecular solids other expressions for  $\bar{\sigma}$  are required.

Electronic processes may also initiate heavy-particle motion, hence sputtering or desorption of atoms from a material. One such process is dissociative recombination in gases, a process resulting in sputtering from small planetary bodies, which will be discussed in the following section (e.g.,  $e + O_2^+ = O + O + \Delta E$ ). Heavy-particle motion, hence sputtering, may be produced in certain nonconducting materials by similar electronic processes or by the coulomb repulsion between closely spaced ions resulting from the incident ionizing radiation, which is thought to produce tracks in insulators. If the cascade density is low, then the energy deposited in heavy-particle motion produced by such processes can be used to determine  $\nu(\Delta E)$  in Eq. (6.41). For example, as the ionization density along a heavy-particle track is  $W_e^{-1} |dE/dz|_e$ , the energy per unit path length available in coulomb repulsion is  $C \cdot (e/W_e)^2 |dE/dz|_e^2$ , where  $C$  is a factor depending on the track width, which varies slowly with energy. The sputtering yield then would have the form  $Y \propto |dE/dz|_e^2 \cdot C$  if charge separation (electrons and ions) is maintained for times of the order of  $10^{-13}$  sec (i.e. the time for the ions to repel a lattice spacing).

Generally, electronic processes would be associated with low-energy cascades, in which case the approximation to  $G(\Delta E, E')$  should be improved [e.g. for thermal cascades, Eq. (6.40) becomes  $\bar{z} \sim .04 (\Delta E/U_0)^{5/3} \bar{\sigma} n_B^{1/3}$ ]. Similarly, if the cascade density produced either by elastic or inelastic processes is high, then sputtering also becomes a thermal process. That is, the cascades deposit energy in overlapping volumes leaving a heated region. The energy of the incident particle is deposited symmetrically in a narrow region about the path, with a hot spike formed at some depth in the material, as indicated by the Bragg curve in Figure 6.7. When the spike depth is large enough that its effect at the surface is negligible, the sputtering yield is determined by the energy density in the cylindrically symmetric part of the track near the surface. This is the case we treat here, with the energy density parametrized by a temperature.

For high energy densities, the heated material can be considered, to a reasonable approximation, to behave locally like a very hot gas. If the temperatures are not very high, little erosion occurs anyway. It is left as an exercise for the reader (Problem 6.6) to show that the flux of particles crossing the material surface from a hot region of temperature  $T$  and at a density equal to the material density,  $n_B$ , is

$$\phi_B \sim n_B kT \exp(-U_0/kT)/(2\pi M_B kT)^{1/2} \quad (6.42)$$

where  $U_0$  is the surface barrier potential, or the sublimation energy of the

material, and  $M_B$  is the mass of the material particles. The sputtering yield can now be written

$$Y = \int_0^\infty dt \int_0^\infty \pi dr^2 \phi_B[T(r, t)] \quad (6.43)$$

where the problem remaining is to determine the temperature as a function of time and radial distance from the track,  $r$ .

Based on the notions developed in treating particle diffusion, the equation for thermal diffusion is

$$\nabla K(T) \nabla T = C(T) \frac{\partial}{\partial t} T \quad (6.44)$$

where  $K(T)$  is the thermal conductivity and  $C(T)$  the heat capacity. For an atomic vapor  $C(T) = \frac{3}{2} n_B k$  and  $K(T)$ , like the diffusion coefficient, depends on the collision frequency. Using mean free path arguments, we have  $K(T) \propto \bar{v} \bar{\sigma}_d$ , which for hard-sphere collisions is proportional to  $T^{1/2}$ . The resulting nonlinear equation for a cylindrically symmetric temperature distribution has the solution

$$T(r, t) = \varepsilon [1 - r^2/3\Delta^2(t)]^{1/2} / \Delta^2(t), \quad \text{and} \quad T = 0 \text{ for } r^2 > 3\Delta^2(t) \quad (6.45)$$

where

$$\Delta^2(t) = \left[ \frac{4K_0}{C} (t + t_0) \varepsilon^{1/2} \right]^{2/3} \quad \text{and} \quad \varepsilon = \frac{1}{\pi C} \left| \frac{dE}{dz} \right|_{\text{eff}}$$

In the above we have written  $K = K_0 T^{1/2}$ , with  $K_0 \approx (k/\bar{\sigma}_d)(2k/M_B)^{1/2}$ , and assumed the distribution had an initial width determined by  $t_0$ . The part of the energy deposited per path length in the region that leads to the sputtering is indicated by  $|dE/dz|_{\text{eff}}$ . For example, for a high density of elastic scatterings,  $|dE/dz|_{\text{eff}} \sim n_B S_n$ . Lastly, in obtaining Eq. (6.45), we required that the total energy be conserved, i.e., for a temperature-independent specific heat

$$\int_0^\infty C T \pi dr^2 = |dE/dz|_{\text{eff}} \quad (6.46)$$

On substituting the calculated temperature profile of Eq. (6.45) into the equation for sputtering, Eq. (6.43), one finds

$$Y = \left[ \left( \frac{dE}{dz} \right)_{\text{eff}}^2 / 8\pi(K_0 L_0^{3/2})(2\pi M_B k L_0)^{1/2} \right] [1 - g(t_0)] \quad (6.47)$$

where  $L_0 = U_0/k$  and

$$g(t_0) = x_0^3 \int_{x_0}^\infty dx e^{-x/x^2}, \quad \text{with } x_0 = L_0/T(0, 0)$$

For a narrow spike (i.e.  $T(0, 0) \gg L$  or  $g(t_0) \approx 0$ ) the expression for sputtering in Eq. (6.47) is quite simple. This occurs if the energy deposited per unit path length is high, as determined by  $|dE/dz|_{\text{eff}} \gg \pi(C_0 L)\Delta^2(0)$ . The  $(de/dz)_{\text{eff}}^2$  factor in Eq. (6.47) does *not* depend on the assumed forms for  $K$  and  $C$ ; it is a result only of the cylindrical symmetry involved. Therefore, as the cascade density increases, collisional sputtering changes from being proportional to  $(dE/dz)$  to being proportional to a higher power of  $(dE/dz)$ . This fact is again independent of the sputtering mechanism.

For frozen gases and alkali-halides it appears that the dominant sputtering mechanism is related to electronic energy deposition,  $S_e$ , rather than to the elastic collision cascade, i.e.  $S_n$ . (Recently, ion-induced desorption of large biological molecules has also been associated with electronic energy deposition in material.) Further, the sputtering yield for frozen gases depends nearly quadratically on  $S_e$ , as in Figure 6.12. Again, as in the biological damage, the initial events probably do not directly eject material. Rather, the electronic events initiate a "hot" spot, are a source of coulomb repulsion, or are responsible for the production of unattached species which diffuse to the surface.

In the following section we apply some of the ideas discussed here to a related problem, the escape of atoms and molecules from a planetary atmosphere. Although the problem is similar, there are some interesting differences, and it provides a transition into discussing some of the atomic and molecular processes occurring in a planetary atmosphere.

## Planetary Escape

Hot atoms in the upper levels of a planetary atmosphere may have enough energy to overcome the gravitational barrier and escape the planet in much the same way atoms sputter or are evaporated from materials. In the latter case the potential barrier is a result of the atomic interactions between the material particles, whereas in the former it is simply the gravitational force of the planet. For the planetary case the conditions for escape, in the absence of other forces, is  $\frac{1}{2}M_B v_B^2 > U$ , where  $U$  is the gravitational potential energy of the particle, and the direction must be "upward,"  $\cos \theta > 0$ . Noting that  $U \sim GM_B M_p / \mathcal{R}_p$ , we see that this condition is the same for rockets and atoms, as the mass,  $M_B$ , cancels. In the above relationship  $M_p$ ,  $\mathcal{R}_p$ , and  $G$  are the planetary mass, planetary radius, and gravitational constant respectively.

Of course rockets and atoms behave rather differently if other effects are included, because of their huge mass differences. Whereas the atmospheric constituents only provide an overall drag force on the rocket, they easily deflect each other or any fast atom. Therefore, escape can only occur from the upper levels of the atmosphere where it is unlikely that an atom or

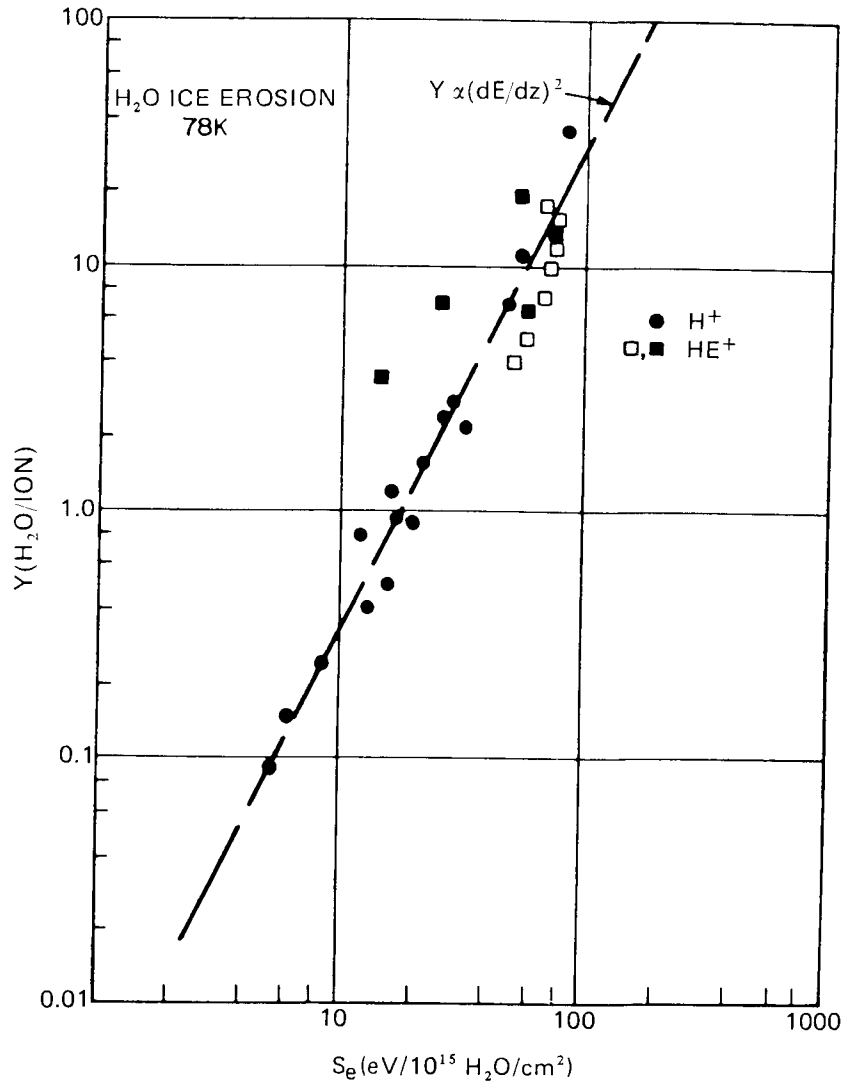


**Figure 6.12.** Sputtering yield versus electronic stopping cross section,  $S_e$ , plotted for incident  $\text{H}^+$  and  $\text{He}^+$ . Dashed line indicates proportionality to the square of the stopping power. [From W. L. Brown, W. M. Augustyniak, L. J. Lanzerotti, R. E. Johnson, and R. Evatt, *Phys. Rev. Lett.* **45**, 1632 (1980).]

molecule will collide with another atom or molecule while exiting the planetary field. This is not unlike the solid-material example we just discussed. It was always assumed for a material that sputtering occurred from the “surface.” For sputtering, the thickness of the “surface” is determined by the depth at which an atom can exit without making another collision. This is clearly of the order of a few mean free paths and therefore a few atomic layers. For metals, Sigmund finds the effective depth of origin to be  $\Delta z = 3/(2n_B \bar{\sigma}_d)$ , using an  $n \rightarrow \infty$  power law for the low-energy collisions. Earlier we showed that the mean projected range for hard-sphere collisions was  $\bar{R}_p = 3/(n_B \sigma_{AB})$ , which, averaged over possible angular directions lead-

ing to escape, would give a similar result for the effective depth of origin of a sputtered particle.

For solid materials it was assumed that the density  $n_B$  was constant up to some plane, the “surface,” where it vanished. However, for an atmosphere,  $n_B$  decreases roughly exponentially [viz. Eq. (1.10)]. Rather than discussing the depth of the material, one therefore considers the density of atoms “stacked” above any particular point. This is referred to as the column density

$$N_B(z) \equiv \int_z^\infty n_B(z') dz' \sim H_B n_B(z) \quad (6.48)$$

where the exponential approximation to the atmospheric density is used [Eq. (1.10)], with  $H_B$  the scale height. The effective column density from which particles will escape is, based on sputtering theory,

$$H_B n_B(z) \sim 3/(2\bar{\sigma}_d) \quad (6.49)$$

This atmospheric region is referred to as the exosphere, for obvious reasons, and this “depth” is called the critical level. Although the escape fluxes often are small, over a geological time period, it is felt that they are very important in determining the evolution of a planet’s atmosphere. In the following we delineate these processes contributing to escape. The separation made is somewhat artificial in that the escaping “hot” atoms may have attained the required kinetic energy by a combination of processes.

Because an atmosphere has a background temperature, due predominantly to heating by the incident solar radiation, there is a probability that any particular atom may have an appropriate velocity to escape. This is roughly equivalent to evaporation from a warm surface and is referred to as Jean’s escape. Using the Maxwell–Boltzmann velocity distribution, the reader can verify that the thermodynamic escape flux in Eq. (6.42), subject to the escape conditions given above, becomes

$$\phi_T \sim n_B (U_c + kT) \exp(-U_c/kT) / (2\pi M_B kT)^{1/2} \quad (6.50)$$

Here,  $U_c = GM_B M_p / \mathcal{R}_c$ , is the gravitational potential energy,  $\mathcal{R}_c$  is the distance from the critical level to the planet center ( $\mathcal{R}_c \sim \mathcal{R}_p$ ),  $n_B$  is the density, and  $T$  is the temperature—all evaluated at the critical level, defined by Eq. (6.49).

In Table 6.2 are listed the escape energies in eV/amu for a number of planetary bodies. Remembering that room temperature corresponds to a mean particle energy of the order of 1/40 eV, it is seen that escape of heavy elements is unlikely from any of the listed bodies. Further, although the upper atmospheres of some planets may attain temperatures of a couple of thousand degrees Kelvin, escape of even hydrogen from a heavy planetary body like Jupiter is unlikely. Bodies as small as the moon, of course, are

known to have lost almost all outgassed material unless there is a continuous source of gas. Using Viking data for Mars, and number densities for O and H estimated by McElroy and others, we see that the thermal escape flux for O, a dominant constituent at high altitudes, is  $\phi_T \sim 10^{-38}$  parts/cm<sup>2</sup>/sec. That is, at the present temperatures, oxygen atom escape is negligible even over long evolutionary time periods. On the other hand,  $\phi_T \sim 10^7$  parts/cm<sup>2</sup>/sec for hydrogen atoms, a rather significant flux. Even though the hydrogen density is much smaller than that of oxygen, the exponential in Eq. (6.50) changes rapidly with particle mass.

The absorption of ultraviolet radiation and, to a much smaller extent, ionization by incident electrons and ions results in the formation of an ionized region, a weak plasma of electrons and ions. As the processes in the upper atmosphere can be considered to be roughly in equilibrium at any time, the plasma density is determined by the balance of the ionization processes with electron-ion recombination. Such processes as  $A^+ + e \rightarrow A + hv$  (radiation recombination) are very slow compared to the molecular process  $AB^+ + e \rightarrow A^* + B^*$  (dissociative recombination) because of the weak coupling between the charged particles and the radiation field. Therefore, a large fraction of the recombination occurs at those altitudes where the molecular ion density is significant. In dissociative recombination the separating atoms attain kinetic energies determined by the exothermicity,  $|Q|$ , and momentum conservation:

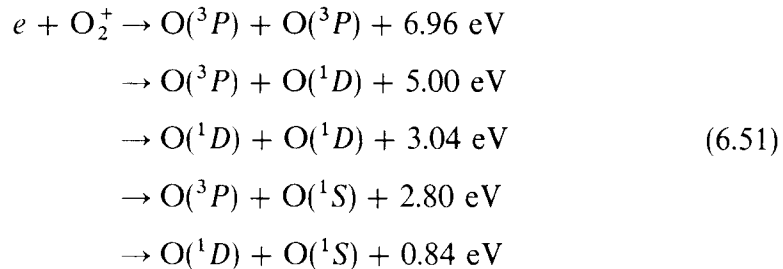
$$E_A = \frac{M_B}{M_A + M_B} |Q| \quad \text{and} \quad E_B = \frac{M_A}{M_A + M_B} |Q|$$

For small planets, where a significant amount of dissociative recombination occurs around the critical level, the dissociation energies may be sufficient for one of the particles to escape the gravitational field of the planet. As the dissociation energies are of the order of a few electron volts, it is clear from Table 6.2 that on the heavier planets not even hydrogen is likely to escape by this process. However, on a planet like Mars, where there is still enough

**Table 6.2.** Escape Energy for Planetary Bodies

Planet or satellite	Escape energy (eV/amu)	Planet or satellite	Escape energy (eV/amu)
Mercury	0.096	Neptune	2.9
Venus	0.56	Moon	0.029
Earth	0.65	Callisto	0.029
Mars	0.13	Ganymede	0.040
Jupiter	19.0	Europa	0.023
Saturn	6.8	Io	0.035
Uranus	2.5	Titan	0.040

gravitational attraction to hold a molecular atmosphere, this escape process probably plays an important role in the evolution of the atmosphere. The ionosphere is predominantly  $O_2^+$  above the critical level, which means that for  $|Q| > 4.2$  eV escape of O is likely. This is the case for the first two of the possible recombination processes listed below:



The escape flux for such processes is calculated from the contributing recombination rates as

$$\phi_e \sim \frac{1}{2} P^e \alpha_i n_i^2 H_i \tag{6.52}$$

where  $n_i$  is the ion number density at the critical level,  $H_i$  the scale height,  $\alpha_i$  the recombination coefficient, and  $P^e$  an escape probability, a number between 0 and 1. In Eq. (6.52) it was assumed, for simplicity, that  $n_e \sim n_i$ ,  $n_e$  being the electron number density. Assuming all recombination occurs by the first two processes (which is not likely viz. Chapter 5),  $P^e \sim 1$ , and using  $\alpha_i$  given in Chapter 5, we find that the average recombination escape flux for O from Mars is  $\phi_e \sim 1 \times 10^7$  parts/cm<sup>2</sup>/sec, obtained by extrapolating the Viking measurements of ion density. This flux, being much larger than that for thermal escape of O and comparable to the thermal escape of H, may control the loss of H<sub>2</sub>O from the Martian atmosphere. Owing to the considerably larger gravitational fields, this process will be unimportant on the Earth and Venus.

Escape can also be driven by particle bombardment. That is, on non-magnetic planets, the solar wind interacts strongly with the upper atmosphere of the planets, and some satellites of the outer planets lie within the planetary radiation belts and are subject to heavy-particle and electron impact. If these incident particles do penetrate into an atmospheric region, then escape due to sputtering is initiated by electronic energy deposition (ionization), as just discussed, and by collision cascades. However, it is known that the upper ionospheric region of a nonmagnetic planet interacts strongly with the solar wind, deflecting a large fraction of the incident particles around the planet via induced fields in much the same way the magnetosphere of the earth deflects the solar wind. Further, as electrons are easily deflected by these field and, in fact, ions do penetrate, a net charging may develop which repels subsequent ions and/or causes ejection of planetary ions. (Such charging, of course, is controlled in a laboratory sputtering

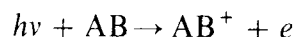
experiment when one irradiates materials with ions.) Fast neutral particles which are impervious to these planetary fields are created if that charge exchange occurs at high altitudes, leaving a slow ion in the magnetic field and a fast neutral directed into the atmosphere. As the resonant and near resonant charge transfer cross sections (e.g.,  $H^+ + H \rightarrow H + H^+$  and  $H^+ + O \rightarrow H + O^+$ ) can be quite large compared to other processes, neutralization may occur at sufficient heights to allow penetration of a significant fraction of the solar wind.

From the above discussion it is apparent that sputtering and/or field ejection due to particle bombardment is quite complex. Estimates for Mars put the escape flux of atoms due to such processes a couple of orders of magnitude below that for thermal ejection of H or recombination ejection of O. On the Galilean satellites of Jupiter, ejection due to particle bombardment either of tenuous "atmospheric" gases, e.g., on Io, or condensed gases on the surfaces of the satellites may be important sources of heavy atoms for the Jovian magnetospheric plasma. Similarly, charged particles or U.V. ejection of molecules from ice grains and comets may be a source of large molecules in space. In the following section we consider some of the chemical processes involved due to ultraviolet irradiation of planets. Whereas the process we have been discussing above affect the atmosphere only over long periods of time, the processes to be discussed determine the day-to-day character of the atmosphere.

## The Ionosphere

Historically the earth's ionosphere has been divided into three major shells in which the ion type, density, and temperature are controlled by various molecular processes. Although the following discussion of these processes is well known and the presentation oversimplified, it still provides a good example of a macroscopic phenomenon controlled by molecular processes. We begin with a brief discussion of solar radiation absorption which initiates the molecular processes occurring in the ionosphere.

In the solar spectrum, radiation of wavelength,  $\lambda$ , less than about 1000 Å is responsible for ionization of atmospheric species. This comprises a very small fraction of the incident radiation. At longer wavelengths dissociation and other molecular processes dominate the absorption of solar energy. Associating a cross section  $\sigma_{\lambda, AB}$  with the ionization process ( $v = c/\lambda$ ,  $c$  being the velocity of light),



where  $h\nu$  is the photon energy, we can express the ionization production as a function of altitude. Assuming a simple exponential, single-species atmos-

where, we write the production rate as

$$\frac{dn_{AB^+}}{dt} = \sigma_{\lambda, AB} n_{AB} I_{\lambda}(z) \quad (6.53)$$

where  $I_{\lambda}$  is the radiation intensity at altitude  $z$ . Neglecting any sources of radiation of wavelength  $\lambda$  that may exist in the atmosphere, we see that the intensity decreases with depth due to absorption, as in Eq. (2.2). That is,

$$I_{\lambda}(z) = I_{\lambda}(\infty) \exp \left[ - \sum_i n_i \sigma_{\lambda i} z_i / \cos \chi_s \right] \quad (6.54)$$

where the sum is over all species in the atmosphere, and  $\chi_s$  is the solar zenith angle, the angle that the incident radiation forms with the vertical. In Figure 6.13 the functions  $dn_{AB^+}/dt$ ,  $I_{\lambda}$ , and  $n_{AB}$  from Eq. (1.10) are illustrated and, as one would expect, the production rate of ions has a maximum. This production profile is often referred to as a Chapman profile. At high altitudes the production decreases like the density of absorbers,  $n_{AB}$ , and at low altitudes it goes to zero because the light intensity has diminished. For small wavelengths, the absorption cross section tends to decrease with decreasing wavelength. Therefore, the maximum ionization production for X-rays tends to occur at a lower altitude than that for ultraviolet light. This is only roughly true, however, as radiation absorption is quite specific, with the absorption cross section for atmospheric molecules being very high (or small) at certain frequencies.

If electron-ion recombination is fast compared to other molecular processes and to diffusion, then from the production profiles one would expect to find a layered ionosphere, with the ionospheric constituents determined by the absorption process. Although one does indeed find such layered

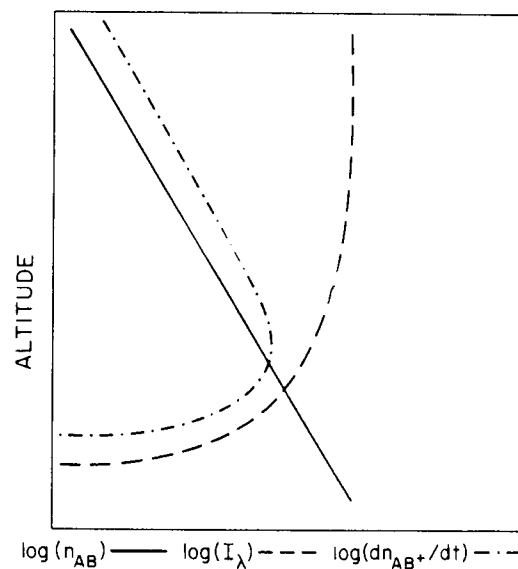


**Figure 6.13.** Schematic diagram of the molecular density,  $n_{AB}$ , incident radiation flux,  $I_{\lambda}$ , and the ion-production rate  $dn_{AB^+}/dt$ .

ionospheres, as indicated in Figure 6.14, the chemical and diffusion processes are not slow and, therefore, the dominant ionic species found is not the ion of the dominant absorbing species in some regions. In the simple photochemical-equilibrium model, a *single* atmospheric molecule, AB, is ionized and recombination,  $e + AB^+ \rightarrow A^* + B^*$ , is assumed to be fast compared to reactions of  $AB^+$  with other species and to diffusion. Assuming charge equilibrium, i.e.,  $n_e = n_{AB^+}$ , with production and recombination in balance, we obtain

$$n_{AB^+}^2 = J_{AB} n_{AB} / \alpha_{AB^+} \quad (6.55)$$

where  $\alpha_{AB^+}$  is the recombination coefficient discussed in Chapter 5, and  $J_{AB}(z) = \sum_{\lambda} \sigma_{\lambda AB} I_{\lambda}(z)$  is the sum over all absorption processes leading to ionization of AB. A situation close to this exists on Mars, but the dominant ion is not the ionic form of the dominant absorbing molecule.

The Martian atmosphere is predominantly  $CO_2$  up to about 200 km where atomic oxygen begins to dominate. The most important ionization processes are  $CO_2 + hv \rightarrow CO_2^+ + e$  and  $CO_2 + hv \rightarrow CO + O^+ + e$  below 230 km and  $O + hv \rightarrow O^+ + e$  above this. However, the molecular pro-

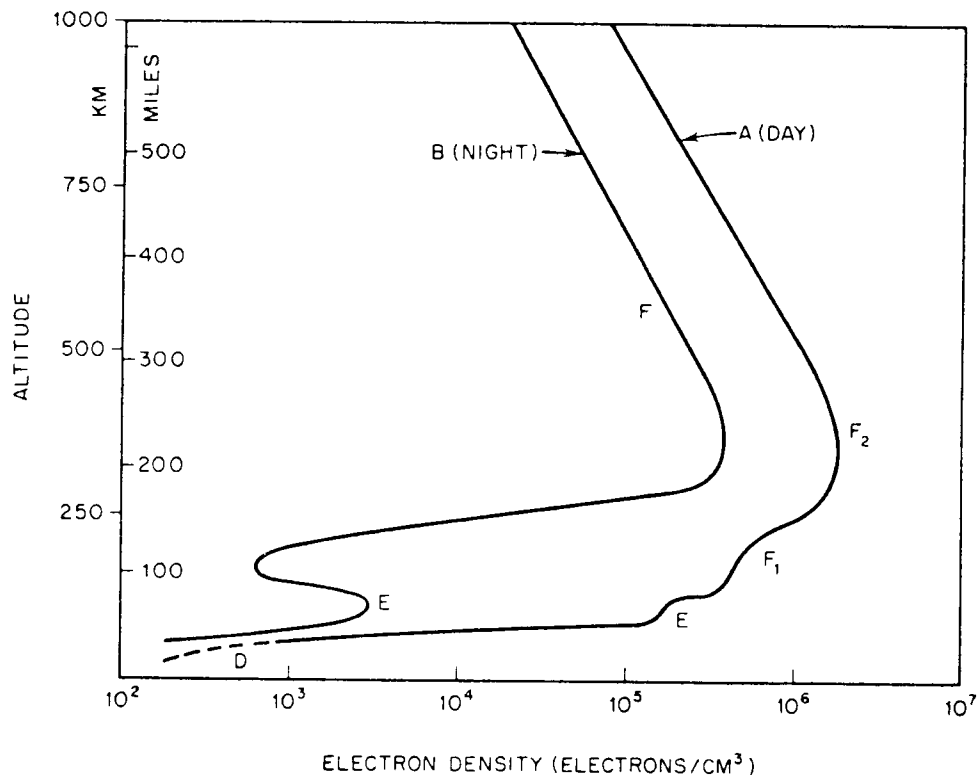
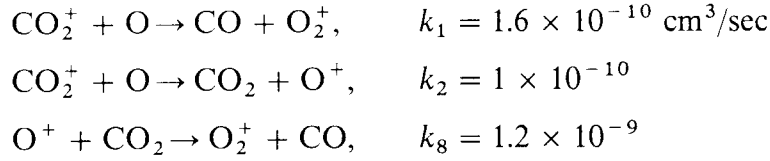
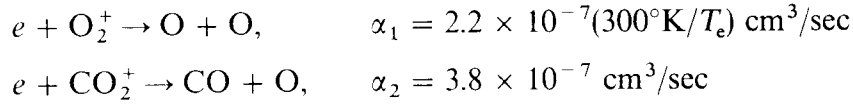


**Figure 6.14.** Electron-density profiles in the earth's atmosphere around the solar maximum. [From S. Glasstone, *Sourcebook on the Space Sciences*, Van Nostrand, New York (1965), p. 487.]

cesses discussed earlier [viz reactions (1), (2), and (8) of Eq. (1.13) and Table 5.2]



are fast compared to recombination as the neutral densities are much larger than the electron and ion densities. It is seen from these equations that both the  $\text{CO}_2^+$  and  $\text{O}^+$  ions rapidly produce  $\text{O}_2^+$ . As the recombination processes



where  $T_e$  is the mean electron temperature, are in turn fast compared to diffusion, the ionosphere is very nearly in photochemical equilibrium. The rate equations, like Eq. (1.14), neglecting diffusion and assuming equilibrium, become

$$\begin{aligned} \frac{\hat{c}}{\hat{c}t} [\text{CO}_2^+] &= 0 = J_{\text{CO}_2} [\text{CO}_2] - (k_1 + k_2) [\text{CO}_2^+] [\text{O}] - \alpha_2 n_e [\text{CO}_2^+] \\ \frac{\partial}{\partial t} [\text{O}^+] &= 0 = J_{\text{O}} [\text{O}] + k_2 [\text{CO}_2^+] [\text{O}] - k_8 [\text{O}^+] [\text{CO}_2] \\ \frac{\partial}{\partial t} [\text{O}_2^+] &= 0 = k_1 [\text{CO}_2^+] [\text{O}] + k_8 [\text{O}^+] [\text{CO}_2] - \alpha_1 n_e [\text{O}_2^+] \end{aligned}$$

In the above equations  $J_{\text{CO}_2}$  and  $J_{\text{O}}$  account for absorption by  $\text{CO}_2$  and  $\text{O}$  for all wavelengths. Using the incident solar spectrum, measured photoionization cross sections, and densities for  $\text{CO}_2$  and  $\text{O}$  with the above rate constants, one obtains the densities of  $\text{O}^+$ ,  $\text{CO}_2^+$ , and the predominant  $\text{O}_2^+$ . As usual, charge equilibrium is also assumed, i.e.,  $n_e = [\text{O}_2^+] + [\text{CO}_2^+] + [\text{O}^+]$ . Calculated ion densities are plotted in Figure 6.15 and compared to Viking I measurements of the ion densities on Mars. An approximate expression for the dominant  $\text{O}_2^+$  density similar to Eq. (6.55) can be found. Noting that  $n_e \approx [\text{O}_2^+] \gg [\text{CO}_2^+]$  and the production of  $\text{CO}_2^+$  is much greater than  $\text{O}^+$ , we obtain

$$[\text{O}_2^+]^2 \sim \frac{J_{\text{CO}_2} [\text{CO}_2]}{\alpha_1} \quad (6.56)$$

Therefore the  $\text{O}_2^+$  density follows the production profile, having a scale height, above the maximum, roughly half the  $\text{CO}_2$  scale height when diffusion is neglected. At higher altitudes than shown here, the ions presumably

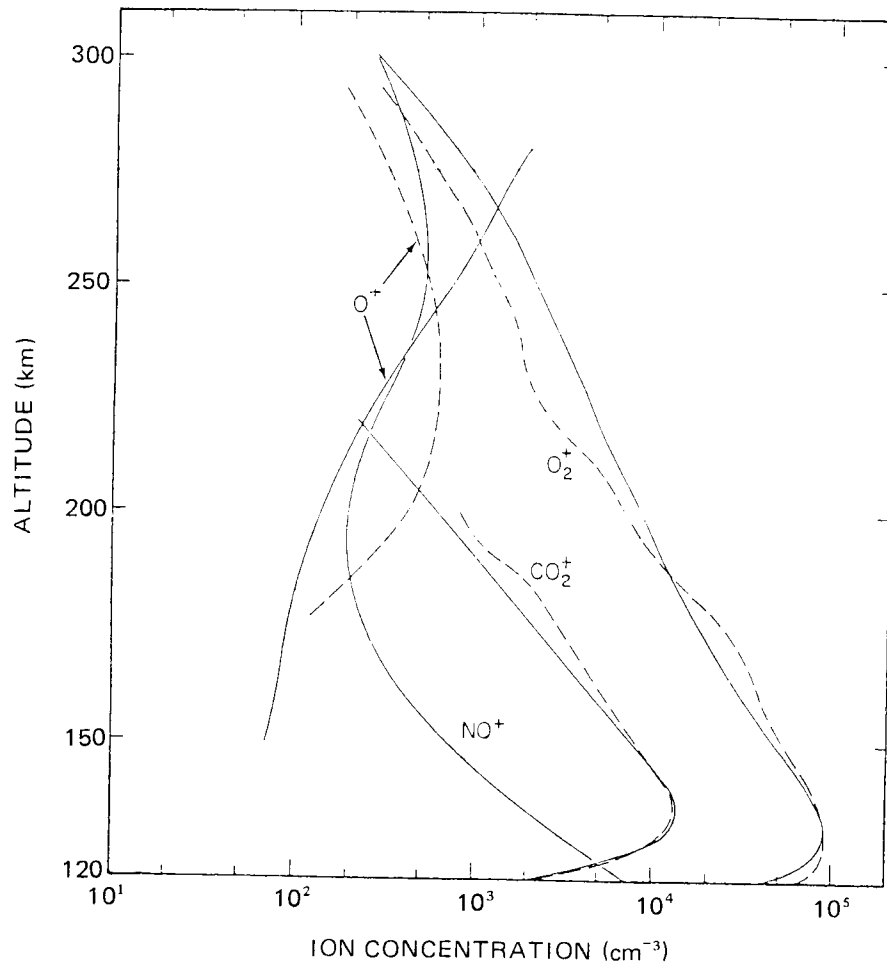


**Figure 6.15.** Ion concentration versus altitude in the Martian atmosphere: dashed lines, Viking I measurements; solid lines, calculation based on chemical rate equations including nitrogen reactions and a solar zenith angle of  $45^\circ$ . [From W. B. Hanson, S. Sanatani, and D. R. Zuccaro, *J. Geophys. Res.* **82**, 4351 (1977).]

attain diffusive equilibrium separately, and at very high altitude the solar wind–ionosphere interaction, discussed earlier, dominates.

The earth's ionosphere differs from that of Mars in that different molecular processes dominate at different altitudes, forming a layered ionosphere as mentioned earlier. We begin with the lowest layer in which ionization is due to hard X-rays and Lyman  $\alpha$  radiation and, hence, is influenced by solar flares. In the so-called *D* region (Figure 6.14), where the molecular densities are large, three-body processes can occur with significant probabilities. For example,  $O_2^-$  is formed by attachment,  $O_2 + X + e \rightarrow O_2^- + X$ . This in turn leads to a significant fraction of the recombination occurring via mutual neutralization,  $A^+ + O_2^- \rightarrow A^* + O_2^*$ . We saw in Chapter 5 that such a process has a large rate coefficient, but the electron is also easily detached by photons or collisions with neutrals. Therefore, although recom-

bination depends on the negative-ion concentration (as well as free-electron concentration), the density of negative ions is controlled by the electron detachment cross sections. Simple theoretical models of the *D* region would predict the presence of varying amounts of  $O_2^+$ ,  $NO^+$ , and  $O_2^-$ . However, measurements show the presence of significant fractions of  $H_3O^+$ ,  $H_5O_2^+$ , and other water vapor ion clusters, as well as  $CO_3^-$ ,  $HCO_3^-$ ,  $NO_3^-$ , and  $CO_4^-$  due to the presence of small amounts of  $CO_2$  and water vapor particularly at the lower levels. The chemistry in this region can, therefore, be quite complex.

In the *E* region ionization proceeds by the following processes: X-rays ( $100 < \lambda < 31 \text{ \AA}$ ) on  $O_2$ ,  $N_2$ , and  $O$ ; ultraviolet in the Lyman continuum ( $\lambda < 910 \text{ \AA}$ ) on  $O_2$  and  $O$ ; and Lyman  $\beta$  (at  $1025.7 \text{ \AA}$ ) on  $O_2$ . However, reactions (3)–(7) in Eq. (1.13) rapidly remove  $N_2^+$  and  $O^+$ , leaving an ionosphere dominated by  $O_2^+$  and  $NO^+$ . In the daytime  $O_2^+$  is the dominant ion, and simple photochemical equilibrium predicts densities

$$[O_2^+]^2 \approx n_e^2 \approx J_{O_2} [O_2] / \alpha_1 \quad (6.57)$$

where  $\alpha_1$  is the recombination coefficient considered earlier. As the effect of solar radiation diminishes in the evening and hence the density of electrons decreases, the recombination process eventually gives way to the charge-exchange process



which controls the removal of  $O_2^+$ . As the recombination process



is relatively slow, the *E* region is eventually dominated by  $NO^+$  ions. Apparently the background radiation of the night sky produces a sufficient amount of  $O_2^+$  to maintain an ionosphere consisting of  $O_2^+$  and  $NO^+$ . It is important to note here that the time constant for decay or formation of the *E* region is still small, so that transport processes for the most part play a small role. From the rate equations, the time constant for loss of  $O_2^+$  is  $\tau \simeq (2\alpha_1 n_e)^{-1}$ , which for values of  $n_e$  in the *E* region is of the order of a few seconds. Therefore, total ion densities closely follow changes in the ion production rate.

In the lower *F* region, the *F*<sub>1</sub> region, the dominant ions produced are  $N_2^+$  and  $O^+$  as the  $O_2$  density is now diminished (i.e., above about 125 km  $[O] > [O_2]$  due to gravitational separation). Invoking the same processes for  $O^+$  and  $N_2^+$  as before, it is clear that  $NO^+$  will be the dominant ion. Allowing removal only via dissociative recombination,  $e + NO^+$ , and production of  $NO^+$  via ionization of  $O$  and reaction with  $N_2$ , one finds

$$\begin{aligned} [O^+] &= J_O [O] / k_4 [N_2] \\ [NO^+] &= \frac{1}{2} [O^+] [(1 + 4J_O [O] / \alpha_3 [O^+]^2)^{1/2} - 1] \end{aligned} \quad (6.58)$$

At higher altitudes the production-to-loss ratio for  $O^+$  in Eq. (6.58) gradually increases due to the differing scale heights for  $N_2$  and  $O$  and the increased intensity of ionizing radiation. The  $O^+$  density eventually dominates  $NO^+$  in the vicinity of 180 km. It is useful to evaluate the time constant for obtaining equilibrium. The reader can verify that, in the absence of diffusion, the equilibrium time constant for losing  $O^+$  is  $\tau = (k_4[N_2])^{-1}$ , which increases with altitude. At 250 km,  $\tau \sim 1/2$  hour, and, therefore, transport processes must begin to be important in determining the character of the ionosphere.

The upper  $F$  region, called the  $F_2$  region, will be dominated by  $O^+$  ions. From our previous discussion both the  $O^+$  density and the time constant increase with increasing altitude. That is, as radiation recombination is very slow, recombination is still controlled by the formation of molecular ions, as it was in the  $F_1$  region. Such an increasing density would not, however, be in gravitational equilibrium; eventually a downward, diffusive flow of ions will occur. As the time constant for recombination increases, this downward flow will become more important, enhancing recombination by bringing  $O^+$  ions into a region of higher  $N_2$  density. An ion density peak will occur when the times for chemical processes become comparable to the characteristic transport times.

To maintain charge equilibrium, small electric fields exist in the ionosphere. By adding such a term to the force equation [Eq. (1.7)] for both electrons and ions, and combining their equations of motions, the reader can verify (Problem 6.11) that the ion diffusive flux in a steady state is

$$n_i w_i = - \frac{1}{M_i v_i} \left( \frac{\partial P_i}{\partial z} + \frac{\partial P_e}{\partial z} + M_i g n_i \right) \quad (6.59)$$

where  $P_i$  and  $n_i$  are the ion pressure and density respectively,  $P_e$  the electron gas pressure, and  $v_i$  the ion-neutral collision frequency; here we have used  $M_i \gg m_e$ . Equation (6.59) can be rewritten in the form

$$w_i = - D_p \left( \frac{1}{n_i} \frac{\partial n_i}{\partial z} + \frac{1}{T_p} \frac{\partial T_p}{\partial z} + \frac{1}{H_p} \right) \quad (6.60)$$

where  $T_p = T_e + T_i$ , the sum of the electron and ion temperatures,  $D_p = kT_p/M_i v_i$ , and  $H_p = kT_p/M_i g$ . In equilibrium, if  $T_p$  is nearly constant, then

$$n_i = n_i^0 \exp[-(z - z_0)/H_p] \quad (6.61)$$

which is the situation achieved at high altitudes up to the exosphere. The reader should note that since the electrons and ions reach equilibrium together, the scale height  $H_p$  is roughly twice the scale height of the parent atom (assuming  $T_i \sim T_e$ ), and, similarly, the effective diffusion constant is increased. This should not be surprising, as an electric field, which was eliminated from the equations, is acting to affect the densities and motion of the ion.

From the discussion in Chapter 5, the ion–neutral collision frequency in Eq. (6.59), is determined by the polarization interaction,  $V = -\alpha_B e^2/2R^4$ ,

$$v_i = 2.6 \times 10^{-9} n_B (\alpha'_B/m')^{1/2} \text{ sec}^{-1} \quad (6.62)$$

where  $\alpha'_B$  is the polarizability,  $\alpha_B$ , in units of  $10^{-24} \text{ cm}^3$ ,  $m'$  is the reduced mass,  $m$ , in amu, and  $n_B$  in  $\text{cm}^{-3}$ . At altitudes where the dominant neutral gas is O the dominant momentum-change process is, however, not elastic scattering but resonant charge exchange, giving an expression for  $v_i$  which is temperature dependent. In resonant charge exchange,  $\text{O}^+ + \text{O} \rightarrow \text{O} + \text{O}^+$ , the ionic species emerges, moving at roughly the speed of the target neutral. Therefore, the momentum change for the ion is approximately  $M_A v$ , as charge transfer takes place predominantly at large impact parameters. Remembering from Chapter 5 that the resonant charge-exchange cross section had the form  $\sigma_{ct}^{1/2} \sim (a - b \log v)$ , the thermally averaged collision frequency integrates to

$$v_i \simeq \frac{8}{3} n_B (8k/\pi M_A)^{1/2} (T_i + T_n)^{1/2} [(a + 3.96b) - b \log_{10}(T_i + T_n)]^2 \quad (6.63a)$$

For  $\text{O}^+ + \text{O}$  this is

$$v_i \sim 4 \times 10^{-12} n_B (T_i + T_n)^{1/2} [11 - 0.7 \log_{10}(T_i + T_n)]^2 \text{ sec}^{-1} \quad (6.63b)$$

with  $T_i + T_n$  in degrees Kelvin and greater than about  $500^\circ\text{K}$ . At lower temperatures the polarization expression in Eq. (6.62) would dominate.

Rather than attempt to solve the diffusion–recombination problem, the above results can be used to estimate a characteristic diffusion time to be compared to the recombination rate. Using the neutral scale height as a characteristic distance over which significant atmospheric changes occur, we can define a characteristic diffusion time  $\tau_d \sim H_n (v_i/g)$ . This time *decreases* as the density of neutrals decreases, which is opposite in behavior to the recombination time discussed earlier. Assuming  $T_i \sim T_n \sim 500^\circ\text{K}$  and O is the dominant molecule, we have  $\tau_d \sim 6 \times 10^{-6} n_O \text{ cm}^3 \text{ sec}$ . This is equal to about a half hour at 250 km in the vicinity of the electron density maximum, or it is comparable to the  $\text{O}^+$  removal time in that region. At higher altitudes the diffusive process becomes much faster than removal of  $\text{O}^+$  via reaction, resulting in a downward transport of ions. At still higher altitudes (the “top-side” ionosphere), the ions seek diffusive equilibrium separately, with the light ions  $\text{H}^+$  and  $\text{He}^+$  gradually becoming more important. In this region the behavior of the ions is to a large extent controlled by the earth’s magnetic field.

## Final Summary

In this book I have presented a broad range of topics related to collision phenomena from processes involving fast ions at MeV energies, as in

(6.44)], and the integral boundary condition, as in Eq. (6.46), to obtain the  $(dE/dz)^2$  dependence for any  $K$  and  $C$ . What is the energy-deposition dependence of sputtering from a spherical spike?

- 6.8. Derive the thermodynamic escape flux in Eq. (6.50) from a planet with an atmosphere at temperature  $T$  and a gravitational energy barrier to escape,  $U_c$ , at the critical level.
- 6.9. Estimate the sputtering yield for a 1-keV proton impinging on an atmosphere consisting primarily of O above the critical height.
- 6.10. Justify the form of the time constants used in the discussion of the earth's ionosphere.
- 6.11. Derive Eq. (6.59) using equations of motion like Eq. (1.7) for the ion and electrons that include a small, vertical electric field.
- 6.12. The sum of all reactions at depth  $z$ , using Eq. (6.22), is  $\int_0^\infty F(z, t)v_R(T)dt$ . Evaluate and discuss when  $v_R \gg 2D/\langle\Delta z^2\rangle$  and  $v_R \ll 2D/\langle\Delta z^2\rangle$ . When  $v_R$  and  $D$  have the same temperature, show this quantity is temperature independent.

### Suggested Reading

Many useful references are included in the figure captions and tables. Others are listed below.

### Radiation Transport: Ranges and Energy Deposition

- A. DALGARNO in *Atomic and Molecular Processes*, ed. D. R. Bates, Academic Press, New York (1962), Chapter 15.
- J. LINDHARD, M. SCHARFF, and H. E. SCHIOTT, *K. Dan. Vidensk. Selsk. Mat. Fys. Medd.* **33**, No. 14, 1 (1963).
- K. B. WINTERBON, *Ion Implantation Range and Energy Deposition Distributions*, Vol. 2, *Low Incident Ion Energies*, Plenum Press, New York (1975).
- P. SIGMUND, *Rev. Roum. Phys.* **17**, No. 7, 823 (1972).
- P. SIGMUND, *K. Dan. Vidensk. Selsk. Mat. Fys. Medd.*, **40**, No. 5, 1 (1978).
- D. W. PALMER, M. W. THOMPSON, and P. D. TOWNSEND, eds., *Atomic Collision Phenomena in Solids*, American Elsevier, New York (1970).
- M. T. ROBINSON and I. M. TORRENS, *Phys. Rev. B*, **9** 5008 (1974).
- P. D. TOWNSEND, J. C. KELLY, and N. E. W. HARTLEY, *Ion Implantation, Sputtering and their Applications*, Academic Press, New York (1976).
- J. JACKSON, J. ROBINSON, and D. THOMPSON, eds., *Atomic Collisions in Solids*, North-Holland, Amsterdam (1980).

### Biological Damage

- R. D. COOPER and R. W. WOOD, eds., *Physical Mechanisms in Radiation Biology*, Technical Information Office, USAEC, Oak Ridge, Tennessee (1974).

- H. DERTINGER and H. JUNG, *Molecular Radiation Biology*, Springer-Verlag, New York (1970).  
 R. A. ROTH and R. KATZ, *Radiat. Res.* **83**, 499 (1980).

### Beam-Foil Transmission Experiments

- I. A. SELLIN and D. J. PEGG, eds. *Beam Foil Spectroscopy*, Plenum, New York (1975).  
 H. G. BERRY, R. DESERIO, and A. E. LIVINGSTON, *Phys. Rev. Lett.*, **41** 1652 (1978).  
 D. S. GEMMEL, *Chem. Rev.*, **80** 301 (1980).  
 J. REMILLIEUX, *Nucl. Inst. and Meth.*, **170** 31 (1980).  
 R. LEVI-SETTI, K. LAM, and T. R. FOX, *Nucl. Inst. and Meth.*, **194**, 281 (1982)

### Sputtering and Thermal Spikes

- D. W. PALMER, M. W. THOMPSON, and P. D. TOWNSEND, eds. *Atomic Collision Phenomena in Solids*, American Elsevier, New York (1970), Session V.  
 P. SIGMUND, *Phys. Rev.* **184**, 383 (1969).  
 P. SIGMUND, in *Proc. Symp. on Sputtering*, Vienna, April 1980, ed. P. Varga et al, (in press).  
 R. D. MACFARLANE and F. TORGENSON, *Science*, **191** 920 (1976).  
 D. A. THOMPSON, R. S. WALKER and J. A. DAVIES, *Rad. Eff.*, **32** 135 (1977).  
 R. Kelley, *Radiat. Eff.*, **32**, 91 (1977).  
 R. BEHRISCH, Sputtering by Particle Bombardment, in *Topics in Applied Physics, Vol. 47*, Springer-Verlag (1981).  
 C. C. WATSON and P. K. HAFF, *J. Appl. Phys.*, **51** 691 (1980).  
 J. B. SANDERS, *Rad. Eff.*, **51** 43 (1980).  
 R. E. JOHNSON and R. EVATT, *Rad. Eff.*, **52** 187 (1980).  
 M. SZYMOSKI, *Rad. Eff.*, **52** 9 (1980).  
 P. SIGMUND and C. CLAUSSEN, *J. Appl. Phys.* **52**, 990 (1981).

### Atmospheres and Escape

- P. M. BANKS and G. KOCKARTS, *Aeronomy*, Parts A and B, Academic Press, New York (1973).  
 J. W. CHAMBERLAIN, *Theory of Planetary Atmospheres*, Academic Press, New York (1978).  
 A. E. S. GREEN and P. J. WYATT, *Atomic and Space Physics*, Addison-Wesley, Reading, Massachusetts (1965).  
 J. C. G. WALKER, in *Atomic Processes and Applications*, ed. G. Burke and B. L. Moiseiwitsch, North-Holland, Amsterdam (1976), Chapter 3.  
 P. K. HAFF and C. C. WATSON, *J. Geophys. Res.* **84**, 8436 (1979).  
 J. FOX and A. DALGARNO, *J. Geophys. Res.*, **84** 7315 (1979).

- H. DERTINGER and H. JUNG, *Molecular Radiation Biology*, Springer-Verlag, New York (1970).  
 R. A. ROTH and R. KATZ, *Radiat. Res.* **83**, 499 (1980).

### Beam-Foil Transmission Experiments

- I. A. SELLIN and D. J. PEGG, eds. *Beam Foil Spectroscopy*, Plenum, New York (1975).  
 H. G. BERRY, R. DESERIO, and A. E. LIVINGSTON, *Phys. Rev. Lett.*, **41** 1652 (1978).  
 D. S. GEMMEL, *Chem. Rev.*, **80** 301 (1980).  
 J. REMILLIEUX, *Nucl. Inst. and Meth.*, **170** 31 (1980).  
 R. LEVI-SETTI, K. LAM, and T. R. FOX, *Nucl. Inst. and Meth.*, **194**, 281 (1982)

### Sputtering and Thermal Spikes

- D. W. PALMER, M. W. THOMPSON, and P. D. TOWNSEND, eds. *Atomic Collision Phenomena in Solids*, American Elsevier, New York (1970), Session V.  
 P. SIGMUND, *Phys. Rev.* **184**, 383 (1969).  
 P. SIGMUND, in *Proc. Symp. on Sputtering*, Vienna, April 1980, ed. P. Varga et al, (in press).  
 R. D. MACFARLANE and F. TORGENSON, *Science*, **191** 920 (1976).  
 D. A. THOMPSON, R. S. WALKER and J. A. DAVIES, *Rad. Eff.*, **32** 135 (1977).  
 R. Kelley, *Radiat. Eff.*, **32**, 91 (1977).  
 R. BEHRISCH, Sputtering by Particle Bombardment, in *Topics in Applied Physics, Vol. 47*, Springer-Verlag (1981).  
 C. C. WATSON and P. K. HAFF, *J. Appl. Phys.*, **51** 691 (1980).  
 J. B. SANDERS, *Rad. Eff.*, **51** 43 (1980).  
 R. E. JOHNSON and R. EVATT, *Rad. Eff.*, **52** 187 (1980).  
 M. SZYMOSKI, *Rad. Eff.*, **52** 9 (1980).  
 P. SIGMUND and C. CLAUSSEN, *J. Appl. Phys.* **52**, 990 (1981).

### Atmospheres and Escape

- P. M. BANKS and G. KOCKARTS, *Aeronomy*, Parts A and B, Academic Press, New York (1973).  
 J. W. CHAMBERLAIN, *Theory of Planetary Atmospheres*, Academic Press, New York (1978).  
 A. E. S. GREEN and P. J. WYATT, *Atomic and Space Physics*, Addison-Wesley, Reading, Massachusetts (1965).  
 J. C. G. WALKER, in *Atomic Processes and Applications*, ed. G. Burke and B. L. Moiseiwitsch, North-Holland, Amsterdam (1976), Chapter 3.  
 P. K. HAFF and C. C. WATSON, *J. Geophys. Res.* **84**, 8436 (1979).  
 J. FOX and A. DALGARNO, *J. Geophys. Res.*, **84** 7315 (1979).